Influence of dislocations on the apparent elastic constants in single metallic crystallites an analytical approach

Dokkum, Jan Steven Van; Bos, C.; Offerman, Sven Erik; Sietsma, Jilt

DOI
10.1016/j.mtla.2021.101178

Publication date
2021

Document Version
Final published version

Published in
Materialia

Materialia 20 (2021) 101178

Contents lists available at ScienceDirect

Materialia

journal homepage: www.elsevier.com/locate/mtla

Full Length Article

Influence of dislocations on the apparent elastic constants in single metallic crystallites: an analytical approach

Jan Steven Van Dokkum[a,*], Cornelis Bos[a,b], Sven Erik Offerman[a], Jilt Sietsma[a]

[a] Department of Materials Science and Engineering, Delft University of Technology, 2628 CD Delft, The Netherlands
[b] Tata Steel Research & Development, P.O. box 10000, CA IJmuiden 1970, The Netherlands

ARTICLE INFO

Keywords:
Dislocation loop
Dislocation structure
Elastic constants
Tensile behaviour
Analytical modelling

ABSTRACT

Intricate knowledge of dislocation networks in metals has proven paramount in understanding the constitutive behaviour of these materials but current experimental methods yield limited information on the characteristics of these networks. Recently, the isotropic anelastic response of metals has been used to investigate complex dislocation networks through the well-known phenomenon that the observed elastic constants are influenced by dislocations. Considering the dependence of the behaviour of a Frank-Read (FR) source on its initial dislocation character and using discerning characteristics of dislocations, i.e. Burgers vector, line sense and slip system, the present paper takes dislocation character, crystal structure and dislocation network geometry into account and obtains the anisotropic mechanical response for a generic Poisson's ratio. In this work, the tensile test tangent moduli and yield points are presented for spatially uniform and nonuniform dislocation distributions across slip systems. First, the reversible shear strain of the FR source is derived as a function of initial dislocation character. The area swept by a mobile and initially straight dislocation segment pinned at both ends is given as an explicit function of the line stress. Secondly, the anisotropic anelastic strain contribution of FR sources to the total pre- and at-yield strain in single crystallites is calculated. For a given normal stress and superposition of the principal infinitesimal linear elastic lattice strain and anelastic dislocation strain, the tangent moduli are presented. The moduli and the inception of plastic flow have a notable dependence on initial dislocation character, spatial dislocation distribution and loading direction.

1. Introduction

It is well-known that the mechanical deformation of metals is chiefly governed by the generation, glide and storage of dislocations. Post-yield mechanical deformation is commonly captured in work hardening models, e.g. Kocks and Mecking [1], Bergström [2,3] and internal-variable models [4,5], which make use of average quantities, e.g. the total dislocation density, average storage distance and average interaction range. Lesser studied is the contribution of dislocations to the pre-yield constitutive behaviour. The nonlinear pre-yield mechanical behaviour, as observed by [6–10], is due to an additional strain component on top of the elastic lattice strain during loading and unloading. First Eshelby [11] and later Koehler and DeWit [6] connected the apparent elastic constants, which are lower than the theoretical constants, to the bowing out of pinned dislocation segments. Knowledge of pre-yield mechanical behaviour has already proven important in the design of forming methods [12], micro-mechanical systems [13] and ultrasonic measurement techniques [14]. An outstanding example is the physical-phenomenological full-field numerical crystal plasticity model of isotropic anelasticity by Torkabadi *et al.* [12]. However, it has not been possible to accurately predict the apparent elastic constants after plastic deformation [9].

At temperatures below about one-third of the melting point of metals, movement of dislocations is the dominant mechanism for anelastic and inelastic deformation [15]. It is widely accepted that under these conditions for single crystallites, the constitutive behaviour is entirely governed by the dynamics of dislocations. A key microstructural feature is the dislocation network. The dislocation structure in the network is complex, with a distribution of dislocation link lengths. Inelastic deformation is considered by treating a dislocation model of the statistical distribution of dislocation link lengths [16]. The probability of release is determined by the link length; only certain link lengths with low line stresses contribute to inelastic deformation [16,17]. Closed-form expressions are found for quasi-static loading conditions, where a range of segments are activated simultaneously [16–19]. Anelastic deformation is governed by the same principles, but for static loading conditions only the longest segments are expected to activate and determine the critical shear stress. However, the Taylor relation [20] still holds on the level

* Corresponding author.
E-mail address: j.s.vandokkum@tudelft.nl (J.S. Van Dokkum).

https://doi.org/10.1016/j.mtla.2021.101178
Received 14 July 2021; Accepted 25 July 2021
Available online 2 August 2021

of single crystallites, which is often interpreted as describing the critical shear stress needed to free (or activate) dislocations with the average segment length [21]. It thus is necessary to use average statistical quantities, which characterize the ensemble of dislocations in the crystallite, when one constructs an elastic-anelastic constitutive model for static loading conditions.

Recently, Van Liempt and Sietsma [8] showed that the pre-yield mechanical behaviour is a measure for the average properties of the dislocation network which they characterized by the total dislocation density and the average dislocation segment length. The method championed by Arechabaleta *et al.* [9,10] allows for obtaining information on the characteristics of a dislocation network via mechanical testing. However, the crystallographic texture of a polycrystalline material is only taken into account by the Taylor factor and the assumed circular dislocation loop shape is only valid for materials with Poisson's ratio $\nu = 0$, i.e. highly compressible materials. Hereby, for one, the model predicts an isotropic anelastic response for Poisson's ratio $\nu \sim 0$, and secondly, retrieves only spatially averaged quantities on a mesoscale.

We envision a dislocation network as a continuous structure consisting of discrete dislocation segments delimited by microstructural features like precipitates, solute atoms, grain boundaries and interaction interacting with adjacent dislocation segments within the same net [10,22]. Those points of interaction, which include all microstructural defects that impede local dislocation motion, are commonly known as pinning points where dislocation motion is locally impeded. The motion of a given dislocation segment, i.e. a straight dislocation line under zero applied shear stress, delimited by pinning points, was first described by Frank and Read and is known as a Frank-Read (FR) source [23]. When the FR source bows out on its glide plane and not yet attains its critical shape, the shear strain contribution is reversible. This reversible strain contribution affects the apparent elastic constants and is termed the anelastic dislocation strain in this work. As the FR source attains its critical shape, the source is activated and the dislocation loop, if unimpeded, keeps expanding. The current definition of "anelastic" and "anelasticity" by Li and Wagoner [24] is adopted here: a mode of deformation that is mechanically recoverable and energetically dissipative, where for metals, nonlinear elasticity is implicit because of the bowing out of pinned dislocation segments. Loading/Unloading hysteresis thus is due to dissipation and the bow-out model captures the anelastic strain for a given stress state in metallic crystallites.

The circular equilibrium shape of the FR source under an applied stress was first discussed by Frank and Read [23], and Schoeck [25]. However, for isotropic linearly elastic materials, it is well-known that the elastic energies per unit segment length of edge and screw dislocations are unequal for a non-zero Poisson's ratio. Therefore, a mixed-character dislocation experiences an aligning torque towards its screw orientation because the self-energy of the edge dislocation is greater than the self-energy of the screw dislocation. Therefore, the equilibrium shape of FR sources in metals is non-circular. Firstly, DeWit and Koehler [26] obtained a parametric function for the static equilibrium shape of the FR source as a function of the self-energy by calculus of variations. Following their seminal work [26], Kovacs [27] formulated a physical yield criterion depending on the initial dislocation character of the FR source. More recently, Cash and Cai [14] investigated the dislocation contribution to acoustic non-linearity in order to non-destructively monitor plastic deformation. They presented an implicit analytical expression for the anelastic dislocation shear strain contribution of initially straight edge and screw segments. Knowing the anelastic shear strain per FR source, Koehler and DeWit [6], and Agrawal and Verma [7] presented in their seminal works the apparent Young's moduli for face-centered and body-centered cubic (FCC and BCC) crystallites, respectively. Nearly all crystals are elastically anisotropic, however the framework that emerges by assuming elastic isotropy is useful and even reasonably accurate for most crystals [28].

Current models [6–10] assume a uniform dislocation distribution over slip systems. Hereby, the models of Refs. [6,7] predict a linear anelastic mechanical response with cubic symmetry. The principal anelastic dislocation strain, however, increases non-linearly with the applied normal stress. Therefore, the tangent modulus is an appropriate measure. The models of Refs. [8–10] predict a non-linear mechanical response but with isotropic symmetry. However, it is trivial that the local response of a given crystallite depends on its spatially uniform or non-uniform dislocation distribution over slip systems. Using discerning characteristics of dislocations, i.e. Burgers vector, line sense and slip system, we take the crystal structure into account and obtain an expression for the anisotropic anelastic mechanical response.

In this work, we present an analytical model of the anisotropic tangent moduli and the yield points for nonuniform dislocation networks in single crystallites. First, the works by DeWit and Koehler [26], and Cash and Cai [14] are extended with an explicit formulation of the area swept by a single FR source as a function of the applied shear stress. We derive an explicit analytical expression for the dislocation character at both pinning points as a function of the line stress. Secondly, the behaviour of crystallites is considered. The dislocation network is described by the dislocation characters, densities and segment lengths per slip system. The spatial correlation is given in discrete terms of dislocation densities with a given character on individual slip systems. The anelastic dislocation strain contribution is derived. Finally, combining the elastic and the anelastic mechanical response, we present the pre- and at-yield mechanical behaviour of crystallites as a function of the loading direction.

A set of convenient formulae is presented, where every simplification is made to find the closed-form expression for the tangent moduli and yield strength of cubic crystals. We are unaware of any other publication which presents such an exhaustive treatise of tangent moduli of cubic crystallites without invoking additional phenomenological assertions as made by e.g. Yoshida *et al.* [29] and Sun and Wagoner [30]. The former [29] include the modulus degradation by varying the instantaneous modulus as an exponential function of strain. The latter [30] propose a Quasi-Plastic-Elastic model, which uses a two-yield-surface plasticity theory; a two-surface constitutive model in which the inner surface defines the transition between the linear and non-linear elasticity and the outer surface gives the yield criteria. Aforementioned models are built based on computational convenience and lack a physical basis [31]. For recent and exhaustive discussions on anelasticity we refer to Torkabadi [31] and Li and Wagoner [24]. Our work is based on the underlying mechanism of dislocation driven anelasticity, which gives a physical prediction with a minimum number of parameters and is computationally convenient as well. The central limitation in present model is that the self-energy must adhere to the form of equivalent elastic constants [32]. Present work though is readily extended to cubic anisotropy following [32–36], which is discussed comprehensively.

In the following, we consider the isotropic response of polycrystalline materials first. Our results for various dislocation densities are compared with the predictions made by Van Liempt and Sietsma [8]. The effects of compressibility and dislocation character on experimentally obtained total dislocation density and effective segment length are presented. Our method is directly applicable for analysis of experiments as preformed by Li and Wagoner [24]. Secondly, the anisotropic response for single crystallites is given and validated with the initial cubic Young's moduli obtained by Koehler and DeWit [6], and Agrawal and Verma [7]. Then, the effects of a heterogeneous dislocation distribution over glide planes on the anisotropic symmetry of the apparent elastic constants and the yield point are discussed. A limit analysis of highly compressible and incompressible solids is performed for initial edge and/or screw character segments. The influences of compressibility and dislocation densities on the initial (apparent) shear modulus are given. Finally, a relevant engineering case is presented with Poisson's ratio $\nu = 1/3$. The feasibility of experimentally obtaining information, more than previously possible, on dislocation networks is discussed. The elastic-anelastic

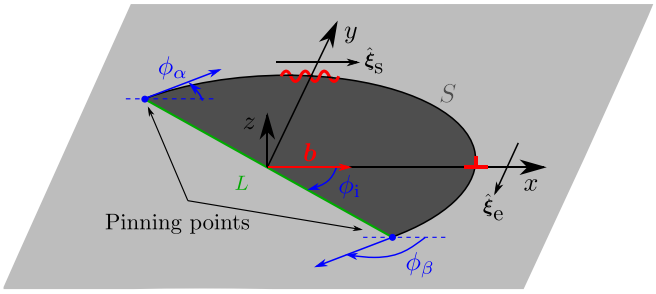

Fig. 1. Schematic representation of a mixed character FR source ϕ_i in the light gray x-y plane with initial segment length L, dark gray swept-out area S and dislocation characters ϕ_α and ϕ_β at the pinning points.

constitutive model takes account of anisotropic effects on a per-grain basis and presents a significant step towards modelling of crystallographically textured cubic materials.

2. Preliminaries and notations

Following Nordmann [37], we apply throughout this work the direct tensor notation. Zeroth-order tensors/scalars are symbolized by italic letters (e.g. a, b, A and B), first-order tensors/vectors by italic lower case bold letters (e.g. $\boldsymbol{a} = a_i \boldsymbol{e}_i$ and $\boldsymbol{b} = b_j \boldsymbol{e}_j$ with basis $\boldsymbol{e}$), second-order tensors by italic uppercase bold letters (e.g. $\boldsymbol{A} = A_{ij} \boldsymbol{e}_i \otimes \boldsymbol{e}_j$ and $\boldsymbol{B} = B_{kl} \boldsymbol{e}_k \otimes \boldsymbol{e}_l$) and fourth-order tensors by italic uppercase bold calligraphic letters (e.g. $\boldsymbol{\mathcal{A}} = A_{ijkl} \boldsymbol{e}_i \otimes \boldsymbol{e}_j \otimes \boldsymbol{e}_k \otimes \boldsymbol{e}_l$). Moreover, the first-order zero tensor is given by an italic lowercase bold letter $\boldsymbol{o}$. In vector-matrix notation, vectors are denoted as upright lowercase sans serif bold letters (e.g, normal $\mathbf{n} = (n_1, n_2, n_3)^\intercal$, with superscript $\bullet^\intercal$ indicating the transpose of $\bullet$) and matrices as upright uppercase sans serif bold letters (e.g. elastic matrix $\mathbf{C}^{\mathrm{el}}$).

For a real-valued Cartesian coordinate system and orthonormal basis, e.g. $\hat{\boldsymbol{e}}_i$, where the overscript $\hat{\bullet}$ indicates a unit vector, and origin $\boldsymbol{o}$, basic operations for tensors used are:

1 The tensor product: $\boldsymbol{a} \otimes \boldsymbol{b} = a_i b_j \hat{\boldsymbol{e}}_i \otimes \hat{\boldsymbol{e}}_j = \boldsymbol{C}$;
2 The double-dot product between two second-order tensors: $\boldsymbol{A} : \boldsymbol{B} = A_{ij} B_{kl} \hat{\boldsymbol{e}}_i \otimes \hat{\boldsymbol{e}}_j : \hat{\boldsymbol{e}}_k \otimes \hat{\boldsymbol{e}}_l = A_{ij} B_{ji} = c$;
3 The double-dot product between fourth- and second-order tensors: $\boldsymbol{\mathcal{A}} : \boldsymbol{B} = A_{ijkl} B_{mn} \hat{\boldsymbol{e}}_i \otimes \hat{\boldsymbol{e}}_j \otimes \hat{\boldsymbol{e}}_k \otimes \hat{\boldsymbol{e}}_l : \hat{\boldsymbol{e}}_m \otimes \hat{\boldsymbol{e}}_n = A_{ijkl} B_{lk} \hat{\boldsymbol{e}}_i \otimes \hat{\boldsymbol{e}}_j = \boldsymbol{C}$.

The Einstein summation convention is used where the Latin indices (e.g. i, j, k, l,... except x, y, z and g) run through the values 1, 2 and 3. Throughout this work, we choose to denote the second-order stress and strain tensors, and derived variables by italic lowercase bold (Greek) letters (e.g. strain tensor $\boldsymbol{\epsilon}$). Finally, for a Bravais lattice with translation vectors $\boldsymbol{t}_i$, crystal direction $[uvw]$ is parallel to direction vector $\boldsymbol{d} = u\boldsymbol{t}_1 + v\boldsymbol{t}_2 + w\boldsymbol{t}_3$.

3. Method

3.1. Frank-Read sources

We consider the differential equation of equilibrium of the Frank-Read (FR) mechanism for the case of a uniform applied shear stress $\boldsymbol{\tau}$, with components: (1) the external applied shear stress $\boldsymbol{\tau}$ doing work on the dislocation; and (2), the potential energy changing as the dislocation bows out. In Fig. 1, an FR source is depicted.

The self-energy per unit length U of a dislocation segment for an elastically isotropic Volterra dislocation is approximated by the addition of pure screw b_s and pure edge b_e Burgers vector components, i.e.

$$U(\phi) \approx U_e + U_s = \frac{\mu^{\mathrm{el}}}{2}\left(\frac{b_e^2}{1-\nu} + b_s^2\right), \tag{1a}$$

with

$$b_s = \|\boldsymbol{b}\| \cos(\phi), \qquad \text{and} \qquad b_e = \|\boldsymbol{b}\| \sin(\phi), \tag{1b}$$

where μ^{el} is the isotropic linear elastic shear modulus, ϕ indicates the dislocation character, i.e. it is the angle between the Burgers vector $\boldsymbol{b}$ and the local unit line-sense $\hat{\boldsymbol{\xi}}$, $\|\bullet\|$ the magnitude of the vector $\bullet$ and ν the Poisson's ratio. Here, the start-finish/right-hand convention is used. Note that long-range elastic interaction and the specific energy associated with the dislocation core are neglected. The line tension model is approximate because it considers the dislocation as a line that carries an energy per unit length along itself, and ignores the long-range interaction between different sections of the dislocation network. Only a single FR source is considered because the long-range interaction scales with the inverse of the range. Hence why line tension and self-interaction are low-order approximations. Self-interaction is the elastic interaction between dislocation segments across the same dislocation line. The exact expression for the dislocation energy involves a double integral along the whole loop [38,39]. In order to attain closed-form analytical expressions, we solely consider line tension. Even with these approximations, the model is able to qualitatively capture physical behaviour of dislocations [28,40], and hence is a useful model.

Following DeWit and Koehler [26], the static equilibrium of the FR source is determined by the method of the calculus of variation. Here, the x-y plane is the glide plane; the initial segment with length L lies along the line $y = x\tan(-\phi_i)$, with initial dislocation character ϕ_i, is centred on the origin $\{0,0,0\}$ and is pinned at each end; the Burgers vector $\boldsymbol{b}$ is parallel to the x-axis; the line sense of a positive edge dislocation is anti-parallel to the y-axis; and, the unit plane normal $\hat{\boldsymbol{n}} \equiv (\hat{\boldsymbol{\xi}}_e \times \boldsymbol{b})/\|\hat{\boldsymbol{\xi}}_e \times \boldsymbol{b}\|$ is parallel to the z-axis, which is defined as the slip system with a Cartesian coordinate system and axes $\{x, y, z\}$. The equilibrium shape of a pinned dislocation for a shear stress τ_{xz} as parametric functions is

$$x(\phi) \equiv \frac{1}{\tau_{xz} b}\left(U(\phi)\sin(\phi) + \frac{\partial U}{\partial \phi}\cos(\phi)\right) + C_1, \tag{2a}$$

and

$$y(\phi) \equiv \frac{1}{\tau_{xz} b}\left(U(\phi)\cos(\phi) - \frac{\partial U}{\partial \phi}\sin(\phi)\right) + C_2, \tag{2b}$$

where C_1 and C_2 are the integration constants. Substituting Eq. (1) in the equilibrium shape Eq. (2), we obtain the normalised FR source shape for a linear elastic isotropic material as

$$\frac{\tau_{xz} x(\phi)}{\mu^{\mathrm{el}} b} = \frac{\left(1 + \nu\cos^2(\phi)\right)\sin(\phi)}{2(1-\nu)} + \frac{\tau_{xz} C_1}{\mu^{\mathrm{el}} b}, \tag{3a}$$

and

$$\frac{\tau_{xz} y(\phi)}{\mu^{\mathrm{el}} b} = \frac{(2 - 3\nu + \nu\cos(2\phi))\cos(\phi)}{4(1-\nu)} + \frac{\tau_{xz} C_2}{\mu^{\mathrm{el}} b}, \tag{3b}$$

where C_1 and C_2 are the x- and y-coordinates of the mid-point of the major and the minor axis of the near-elliptical equilibrium shape, respectively. Here, the x- and y-coordinates are normalized with twice the seminal radius of curvature, which for a dislocation with character-independent energy ($\nu = 0$) by Schoeck [25] is the parametric function of a circle with radius $R = \mu^{\mathrm{el}} b/(2\tau_{xz})$. As the shear stress τ_{xz} increases, the radius of curvature of the dislocation loop decreases. The bowing out of a FR source becomes critical when the applied shear stress equals the seminal maximum line stress $\tau_c = \mu^{\mathrm{el}} b/L$. At shear stresses higher than the critical shear stress τ_c, the dislocation line stress $\mu^{\mathrm{el}} b/(2R)$ does not compensate the applied shear stress and the FR source is activated. The mixed character FR source in Fig. 1 is depicted for the critical shear stress τ^c_{xz}, by Kovacs [27]. Kovacs defined the critical shear stress τ^c_{xz} as the line stress τ_{xz} at which a diameter of the equilibrium shape coincides with the initially straight dislocation segment, i.e. $C_1 = C_2 \equiv 0$. The critical stress τ^c_{xz} is a function of the initial dislocation character ϕ_i and Poisson's ratio ν as well.

In order to calculate the anelastic dislocation shear strain contribution per FR source, the area S swept by the source is needed. The area enclosed by the initial and bowed-out segment is

$$S(\tau_{xz}) = \frac{1}{2}\int_{\phi_\beta(\tau_{xz})}^{\phi_\alpha(\tau_{xz})} \left(x(\phi')\frac{\partial y(\phi')}{\partial \phi'} - y(\phi')\frac{\partial x(\phi')}{\partial \phi'} \right) \mathrm{d}\phi', \tag{4}$$

where ϕ_α and ϕ_β represent the dislocation characters at the pinning points $\{x_\alpha, y_\alpha\}$ and $\{x_\beta, y_\beta\}$, respectively (See Fig. 1). To calculate the swept area, the dislocation characters ϕ_α and ϕ_β as a function of the line stress τ_{xz} are needed. The dislocation line stays attached to both pinning points when bowing out. The equilibrium shape must pass through $\{x_\alpha, y_\beta\}$ and $\{x_\beta, y_\beta\}$, which serves as physical boundary conditions to find the coordinates of the mid-point of the major and the minor axis of the near-elliptical equilibrium shape $\{C_1, C_2\}$. The two trigonometric polynomials, which relate the x- and y-distance between pinning points and the line stress, are formulated, i.e.

$$\frac{\tau_{xz} L \cos(\phi_\mathrm{i})}{\mu^\mathrm{el} b} = \frac{\tau_{xz} x(\phi_\beta)}{\mu^\mathrm{el} b} - \frac{\tau_{xz} x(\phi_\alpha)}{\mu^\mathrm{el} b}, \tag{5a}$$

and

$$\frac{\tau_{xz} L \sin(\phi_\mathrm{i})}{\mu^\mathrm{el} b} = \frac{\tau_{xz} y(\phi_\alpha)}{\mu^\mathrm{el} b} - \frac{\tau_{xz} y(\phi_\beta)}{\mu^\mathrm{el} b}. \tag{5b}$$

The domain of dislocation characters ϕ_α and ϕ_β at the pinning points is shifted to $[-\pi, \pi]$ by defining the difference angles $\Delta\phi_\alpha \equiv \phi_\mathrm{i} - \phi_\alpha$ and $\Delta\phi_\beta \equiv \phi_\beta - \phi_\mathrm{i}$. Inspecting Eq. (5), we find that $\Delta\phi_\alpha = \Delta\phi_\beta$ for $\phi_\mathrm{i} = 0$, $\pi/2$, π and $3\pi/2$. Hence the axes of symmetry for an initial screw dislocation segment, with $\phi_\mathrm{i} = 0$ and π, is the line $x = 0$ and for an initial edge dislocation, with $\phi_\mathrm{i} = \pi/2$ and $3\pi/2$, the line $y = 0$. The Peach-Koehler force is parallel to the outward normal of each infinitesimal dislocation segment within the FR source and the newly created dislocation lines, on either half of the expanding loop, have the same self-energy. Hereby, the coordinate of the integration constant is $C_1 = 0$ for initial screw dislocation segments and $C_2 = 0$ for initial edge character segments [40].

Substituting Eqs. (3a) and (3b) into Eqs. (5a) and (5b), we obtain the relationship between the line stress, τ_{xz}, and the dislocation characters at both pinning points, ϕ_α and ϕ_β, by

$$\begin{aligned}\frac{(1-\nu)\tau_{xz} L}{\mu^\mathrm{el} b}\cos(\phi_\mathrm{i}) = \frac{1}{2}\big(&\sin(\phi_\beta)\big(1+\nu\cos^2(\phi_\beta)\big)\\ &-\sin(\phi_\alpha)\big(1+\nu\cos^2(\phi_\alpha)\big)\big);\end{aligned} \tag{6a}$$

$$\begin{aligned}\frac{(1-\nu)\tau_{xz} L}{\mu^\mathrm{el} b}\sin(\phi_\mathrm{i}) = \frac{1}{4}\big(&\cos(\phi_\alpha)\big(2-3\nu+\nu\cos(2\phi_\alpha)\big)\\ &-\cos(\phi_\beta)\big(2-3\nu+\nu\cos(2\phi_\beta)\big)\big).\end{aligned} \tag{6b}$$

The Kovacs condition, which indicates where the applied stress becomes critical [27], reads

$$\Delta\phi_\alpha^\mathrm{c} + \Delta\phi_\beta^\mathrm{c} = \pi, \tag{7}$$

where $\bullet^\mathrm{c}$ indicates the dependent variable $\bullet$ for the critical shear stress τ_{xz}^c. Substituting $\Delta\phi_\alpha^\mathrm{c}$, $\Delta\phi_\beta^\mathrm{c}$ and Eq. (7) into Eqs. (6a) and (6b), we obtain the relationships between the critical shear stress and the dislocation characters at both pinning points as

$$\frac{(1-\nu)\tau_{xz}^\mathrm{c} L}{\mu^\mathrm{el} b}\cos(\phi_\mathrm{i}) = \sin\left(\phi_\mathrm{i}+\Delta\phi_\beta^\mathrm{c}\right)\left(1+\nu\cos^2\left(\Delta\phi_\mathrm{i}+\phi_\beta^\mathrm{c}\right)\right); \tag{8a}$$

$$\frac{(1-\nu)\tau_{xz}^\mathrm{c} L}{\mu^\mathrm{el} b}\sin(\phi_\mathrm{i}) = -\frac{1}{2}\cos\left(\phi_\mathrm{i}+\Delta\phi_\beta^\mathrm{c}\right)\left(2-3\nu+\nu\cos\left(2\left(\phi_\mathrm{i}+\Delta\phi_\beta^\mathrm{c}\right)\right)\right). \tag{8b}$$

By solving Eqs. (8a) and (8b) simultaneously with a semi-analytical method, we find the critical values of the difference angles $\Delta\phi_\alpha^\mathrm{c}$ and $\Delta\phi_\beta^\mathrm{c}$, and critical shear stress τ_{xz}^c. The critical shear stress and associated difference angles are shown in Fig. 2. Similarly, character angles ϕ_α and ϕ_β are calculated as a function of line stress τ_{xz} with a generic initial dislocation character $\phi_\mathrm{i} \in (-\pi, \pi]$. Knowing the critical shear stresses τ_{xz}^c, we obtain difference angles $\Delta\phi_\alpha$ and $\Delta\phi_\beta$ as functions of τ_{xz} from Eqs. (6a) and (6b).

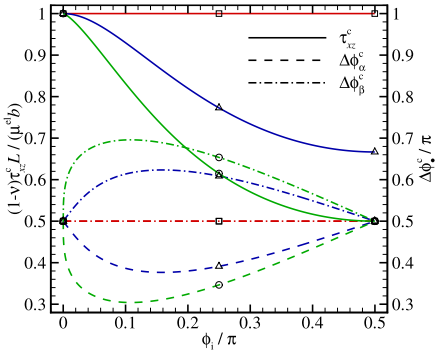

Fig. 2. The normalized critical shear stress $(1-\nu)\tau_{xz}^\mathrm{c} L/(\mu^\mathrm{el} b)$, the normalized critical difference angles $\Delta\phi_\alpha^\mathrm{c}/\pi$ and $\Delta\phi_\beta^\mathrm{c}/\pi$ as functions of normalized initial character ϕ_i/π for different Poisson's ratios $\nu = 0$ 1/3 and 1/2. The values at $\phi_\mathrm{i} = 0, \pi/4$ and $\pi/2$ for $\nu = 0, 1/3$ and $1/2$ are presented as square, triangle and circle symbols, respectively.

The difference angle $\Delta\phi_\mathrm{s}$ is defined as the monotonically increasing difference between the initial right-hand side (RHS) screw dislocation character, i.e. $\phi_\mathrm{i} \equiv 0$, and the dislocation characters $\phi_\alpha = -\Delta\phi_\mathrm{s}$ and $\phi_\beta = \Delta\phi_\mathrm{s}$. Substituting the definition of $\Delta\phi_\mathrm{s}$ in Eq. (6a), we obtain the normalised dislocation line stress as

$$\frac{\tau'_{xz}}{\tau_\mathrm{c}} = \big(1+\nu\cos^2(\Delta\phi_\mathrm{s})\big)\sin(\Delta\phi_\mathrm{s}), \tag{9}$$

with the scaled shear stress $\tau'_{xz} \equiv \tau_{xz}(1-\nu)$ and the range for τ'_{xz}/τ_c is $[-1, 1]$. Since $\cos^2(\Delta\phi_\mathrm{s}) \equiv \cos^2(\pi - \Delta\phi_\mathrm{s})$ and $\sin(\Delta\phi_\mathrm{s}) \equiv \sin(\pi - \Delta\phi_\mathrm{s})$, there are two branches of the solution for $\Delta\phi_\mathrm{s}$ as a function of shear stress τ_{xz}. The dislocation bows out under a given applied shear stress $\tau_{xz} < \tau_{xz}^\mathrm{c}$. The diameter of the equilibrium shape is larger than the length of the initial dislocation segment with difference angle $0 \le \Delta\phi_\mathrm{s} < \pi/2$. When the applied shear stress (originally $\tau_{xz} < \tau_{xz}^\mathrm{c}$) is subsequently removed, the bowed-out RHS screw dislocation returns to its original configuration parallel to the line $x = 0$. Hence the process is reversible. The corresponding branch with solutions $\Delta\phi_\mathrm{s}^\mathrm{stable}(\tau'_{xz}) < \pi/2$ is designated as "*stable*" because the swept-out area will only increase with increasing applied shear stress. This reversibility causes the pre-yield behaviour of FR sources. Secondly, for an applied shear stress τ_{xz} equal to the critical shear stress τ_{xz}^c, the diameter of the equilibrium shape coincides with the initial dislocation segment, i.e. the difference angle $\Delta\phi_\mathrm{s} = \pi/2$. When the applied shear stress (originally $\tau_{xz} = \tau_{xz}^\mathrm{c}$) is subsequently increased, the bowed-out dislocation line does not return to its initial configuration but keeps on expanding with difference angle $\pi/2 < \Delta\phi_\mathrm{s} \le \pi$. The corresponding branch of the solution $\Delta\phi_\mathrm{s}^\mathrm{unstable}(\tau'_{xz}) \ge \pi/2$ is designated as "*unstable*" because the swept-out area will increase. This is the at- and post-yield behaviour of FR sources, which leads to plastic deformation and dislocation multiplication. Here $\tau_{xz} = \tau_{xz}^\mathrm{c}$ is part of the "*unstable*" solution because, although static equilibrium is attained, a small stress perturbation leads to the unstable state of continuing plastic deformation. Finally, it is trivial that $\Delta\phi_\mathrm{s}^\mathrm{unstable}(\tau'_{xz}) = \pi - \Delta\phi_\mathrm{s}^\mathrm{stable}(\tau'_{xz})$.

The explicit equation of the difference angle for the stable equilibrium shape is

$$\Delta\phi_\mathrm{s}^\mathrm{stable} \equiv \sin^{-1}\left(2\sqrt{\frac{1+\nu}{3\nu}}\sin\left(\frac{1}{3}\sin^{-1}\left(\frac{3\sqrt{3\nu}}{2(\nu+1)}\frac{1}{\sqrt{(\nu+1)}}\frac{\tau'_{xz}}{\tau_\mathrm{c}}\right)\right)\right), \tag{10a}$$

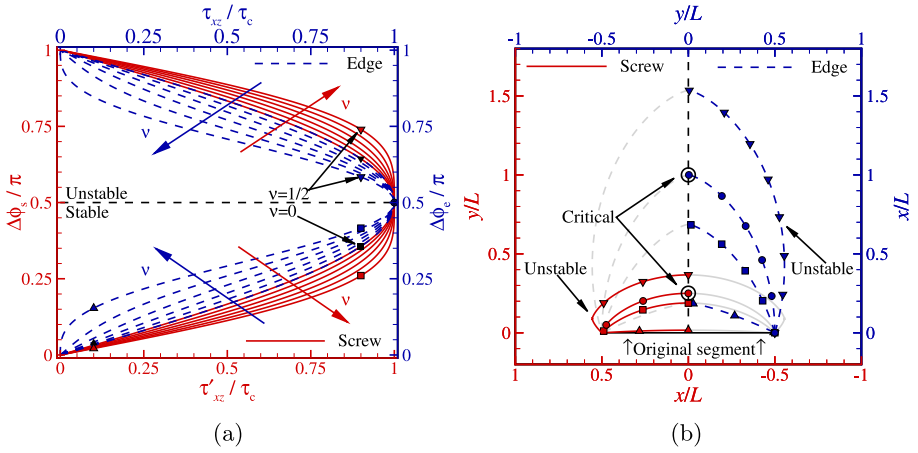

Fig. 3. (a) The normalised difference angles $\Delta\phi_s/\pi$ and $\Delta\phi_e/\pi$ as a function of the normalised line stresses τ'_{xz}/τ_c and τ_{xz}/τ_c for Poisson's ratios ν = 0, 1/10, 1/5, 3/10, 2/5 and 1/2. The coloured arrows indicate an increase in Poisson's ratio ν across equivalently coloured lines. (b) The normalised half equilibrium shapes $\{x/L, y/L\}$ with shear stresses $\tau_{xz}/\tau_c = \tau'_{xz}/\tau_c$= 1/10, 9/10 and 1, and Poisson's ratio ν = 1/2.

for $\nu \neq 0$. In the limit $\nu \to 0$ the difference angle for the stable equilibrium shape is given by

$$\Delta\phi_s^{\text{stable}} \equiv \sin^{-1}\left(\frac{\tau_{xz}}{\tau_c}\right), \tag{10b}$$

in agreement with Eq. (9). Secondly, the difference angle $\Delta\phi_e$ is defined as the monotonically increasing difference between the initial positive edge dislocation character, i.e. $\phi_i \equiv \pi/2$, and the characters $\phi_\alpha = \pi/2 - \Delta\phi_e$ and $\phi_\beta = \pi/2 + \Delta\phi_e$. Substituting the definition of $\Delta\phi_e$ in Eq. (6b), we obtain the normalised dislocation line stress as

$$\frac{\tau_{xz}L}{\mu^{\text{el}}b} = \frac{\left(2+3\nu-\nu\cos(2\Delta\phi_e)\right)\sin(\Delta\phi_e)}{2(1-\nu)} \equiv \frac{\tau_{xz}}{\tau_c}. \tag{11}$$

The explicit equation of the difference angle for the stable equilibrium shape is

$$\Delta\phi_e^{\text{stable}} \equiv \sin^{-1}\left(2\sqrt{\frac{1-2\nu}{3\nu}}\sinh\left(\frac{1}{3}\sinh^{-1}\left(\frac{3\sqrt{3\nu}}{2(1-2\nu)}\sqrt{\frac{(1-\nu)^2}{1-2\nu}}\frac{\tau_{xz}}{\tau_c}\right)\right)\right). \tag{12a}$$

for $\nu \neq 0$ and $\nu \neq 1/2$. Note that for Poisson's ratio $\nu = 0$, Eq. (10b) holds. Since $\cos(2\Delta\phi_e) \equiv \cos\left(2(\pi - \Delta\phi_e)\right)$, again two branches of the solution for $\Delta\phi_e$ are $\Delta\phi_e^{\text{unstable}}(\tau_{xz}) \equiv \pi - \Delta\phi_e^{\text{stable}}(\tau_{xz})$. In the limit $\nu \to 1/2$ the difference angle for the stable equilibrium shape is

$$\Delta\phi_e^{\text{stable}} \equiv \sin^{-1}\left(\sqrt[3]{\frac{\tau_{xz}}{\tau_c}}\right). \tag{12b}$$

Intermediate steps in the derivation of Eqs. (10) and (12) are given in Appendix A.2.

In Fig. 3a, the difference angles as a function of the line stress are presented. The difference angles for line stresses $\tau_{xz}/\tau_c = \tau'_{xz}/\tau_c$= 1/10, 9/10 and 1 are indicated with triangle, square, circle and gradient symbols with Poisson's ratios $\nu = 0$ in black and for $\nu = 1/2$ in red and blue in Fig. 3. The gradient symbols correspond to an unstable static equilibrium solution with normalised line stress $\tau_{xz}/\tau_c = \tau'_{xz}/\tau_c$= 9/10. In the following, the equilibrium shapes and swept-out areas for these stresses and Poisson's ratios are studied in more detail.

In Appendix A.1, the equations for the equilibrium shape of a given FR source as a function of the angles ϕ_α and ϕ_β are given. Hereby, the static equilibrium shape of a given FR source $\{x(L,\tau_{xz}), y(L,\tau_{xz})\}$ as an explicit function of the line stress is obtained. In Fig. 3b, the equilibrium shapes of the FR sources with RHS screw and positive edge character are presented for Poisson's ratio $\nu = 1/2$. Since the shapes are symmetric, half is shown in colour, half in grey. The triangle and square symbols indicate the stable shapes, the circle symbols the critical shapes and the gradient symbols the unstable shapes. These symbols indicate the shapes for the line stresses $\tau_{xz}/\tau_c = \tau'_{xz}/\tau_c$= 1/10, 9/10 and 1 as indicated in Fig. 3a. When the applied shear stress increases so does the circumference of the FR source and the swept-out area S. For Poisson's ratio $\nu = 1/2$, the equilibrium shapes are markedly different between initial RHS screw and initial positive edge FR sources. For isotropic elasticity, the energy per unit edge character line length is a factor $1/(1-\nu)$ times higher than that for pure screw character. This is why the dislocation line aligns towards a majority of screw character and line length with edge character is minimised. However, because the dislocation line must remain continuous, locally sharp corners appear for both "*stable*" and "*unstable*" geometries with increased Poisson's ratio ν. As expected for the maximum dislocation line stress [27], the given diameter of the critical equilibrium shape coincides with the initial dislocation segment, i.e. $\Delta\phi_s = \pi/2$ and $\Delta\phi_e = \pi/2$. Dislocation dynamics governs line shape under quasi-static loading conditions in both the "*stable*" and "*unstable*" regime. However, for static loading conditions, we show in [40] that the dislocation loop orients in the lowest line-tension direction as well when self-interaction is included. When the applied stress is increased beyond the critical shear stress τ^c_{xz}, the FR source continues to expand as depicted by the (dashed) lines with gradient symbols in Fig. 3b. This leads to the well known dislocation multiplication mechanism. Note that once the critical stress is exceeded, no stable quasi-static equilibrium is attained. The time-dependent relation can solely be found solving the inherently dynamic problem. However, the tendency of the dislocation loop to orient itself in the lowest self-energy direction remains. This is only captured by the unstable quasi-static equilibrium solution, which also represents the shape for $\tau_{xz} > \tau^c_{xz}$. Notwithstanding, the present unstable equilibrium solution is relevant beyond purely theoretical interest. We repeat the realistic numerical calculations by Fitzgerald *et al.* [36], for isotropic elasticity [40]. Long-range elastic interaction across the dislocation loop is incorporated. The line tension model is qualitatively consistent with the results which include self interaction [28,40]. The self interaction suppresses the bowing out of the FR source. As a result, for the same magnitude of applied shear stress, the inclusion of long-range interaction reduces the swept out area. It is demonstrated that loops remain "*stable*" even when the applied stress surpasses the maximum dislocation line stress by about a factor two. The FR source attains static equilibrium beyond the approximate half-ellipse shape. Secondly, we reason that within a dislocation network, activated FR sources will experience long-range stresses from adjacent dislocation segments. These stresses are known as back stresses and allow for attaining a equilibrium with dislocation loop shapes comparable to the unstable equilibrium.

The area swept by a given FR source as a function of the difference angles is given in Appendix A.3. Combining Eqs. (10) and (12), and Eqs. (A.14) and (A.15), respectively, we obtain the explicit equation for the swept area $S(\tau_{xz})$. For the sake of brevity, only two limiting cases

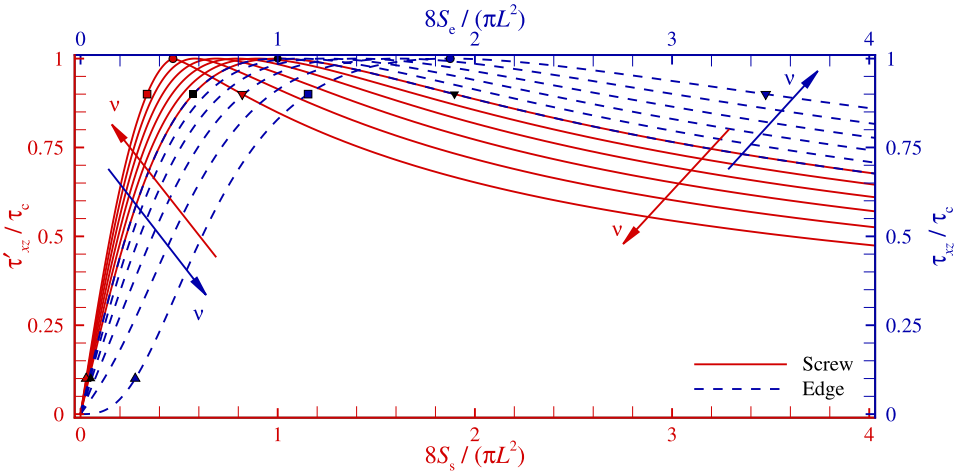

Fig. 4. The normalised line stresses τ'_{xz}/τ_c and τ_{xz}/τ_c as a function of the normalised swept-out areas $8S_s/(\pi L^2)$ and $8S_e/(\pi L^2)$ for Poisson's ratios $\nu = 0,\ 1/10,\ 1/5,\ 3/10,\ 2/5$ and $1/2$. The arrows indicate an increase in Poisson's ratio ν across equivalently coloured lines, from $\nu = 0$ to $1/2$.

are given, namely the positive edge segment and only the normalised areas for the stable equilibrium shape, being

$$\frac{S(\tau_{xz})}{L^2} = \frac{1}{8(\tau_{xz}/\tau_c)^2}\left(2\sin^{-1}\left(\frac{\tau_{xz}}{\tau_c}\right) - \sin\left(2\sin^{-1}\left(\frac{\tau_{xz}}{\tau_c}\right)\right)\right), \tag{13a}$$

and

$$\frac{S_e(\tau_{xz})}{L^2} = \frac{1}{128(\tau_{xz}/\tau_c)^2}\left(60\sin^{-1}\left(\sqrt[3]{\frac{\tau_{xz}}{\tau_c}}\right) - 45\sin\left(2\sin^{-1}\left(\sqrt[3]{\frac{\tau_{xz}}{\tau_c}}\right)\right)\right.$$
$$\left. -9\sin\left(4\cos^{-1}\left(\sqrt[3]{\frac{\tau_{xz}}{\tau_c}}\right)\right) - \sin\left(6\sin^{-1}\left(\sqrt[3]{\frac{\tau_{xz}}{\tau_c}}\right)\right)\right), \tag{13b}$$

for $\nu = 0$ and $1/2$, respectively. In Fig. 4, the dislocation line stress is presented in relation with the swept area. The axes are chosen as such to readily relate with tensile curves, but note that hardening is not considered here. The calculated stress is the stress needed to accomplish plastic strain by a single dislocation loop. The triangle, square, circle and gradient symbols in Fig. 4 correspond to those in Fig. 3. We observe that the area-to-stress relation has a continuously changing slope and zero gradient for the critical shear stress τ^c_{xz}. Initially the dislocation line stress increases with swept area S. The line stress increase depends on the Poisson's ratio ν and is largest for an initial screw dislocation segment because mixed character dislocation line is formed upon expansion of the dislocation loop. *Vice versa*, the dislocation loop of an initial edge character FR source easily expands, which gives rise to a high $\partial S/\partial\tau_{xz}$. Secondly, the local gradient of the area-to-stress relation depends on the length and orientation of the formed dislocation line. The length of the loop with a majority of edge character is minimized while the formation of predominant screw character dislocation lines requires less work (See Fig. 3b). However, given that the dislocation line cannot terminate within the bulk of the material, parts of the loop must attain orientations with higher self-energy. Hereby, the dislocation line stress increases rapidly upon the formation of approximately pure edge character dislocation line as witnessed between the red square and circle symbols in Fig. 4 ($0.9 \leq \tau'_{xz}/\tau_c \leq 1$). And, contrary, an initial edge character FR source sweeps a large area between shear stresses $0.9 \leq \tau_{xz}/\tau_c \leq 1$ (the blue square and circle symbols in Fig. 4). The unloading curve will be the same as the loading curve because dissipation is not taking place in the static solution here. It should be noted that the present model reproduces the anelastic strain for a given stress state but not the symmetric unloading/loading curves as reported in *e.g.* [8–10,24]. The maximum dislocation line stress is highest for screw character FR sources because a pure edge character dislocation line is formed. Once the applied stress matches the critical shear stress, the line stress reduces upon further expansion of the dislocation loop. The dislocation loop will expand and the potential energy is minimized. This "*unstable*" line stress equals the minimum applied stress needed for the loop to continue expanding. Unimpeded expansion of the loop results in softening which is expected when a single FR source is considered and work-hardening is excluded.

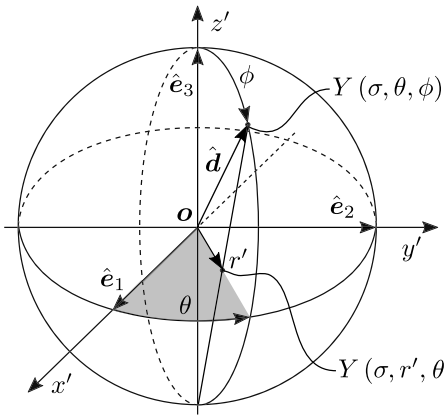

Fig. 5. Schematic representation of the tangent modulus Y on a unit sphere in the crystal frame and the stereographic projection onto the plane with its normal parallel to $\hat{e}_3$ containing the origin o.

3.2. Strain in uniaxially loaded crystallites

For an arbitrary stress $\boldsymbol{\sigma}$ in the crystal frame, the corresponding strain ϵ is a superposition of the elastic and anelastic strains, ϵ^{el} and ϵ^{an}, respectively. The crystal frame is a Cartesian coordinate system with axes $\{x', y', z'\}$ with right-hand orthonormal basis $\hat{e}_i \| t_i$. In Fig. 5, a schematic representation of the crystal frame is given.

The second-order elastic lattice strain tensor ϵ^{el} is derived through a linear mapping of the infinitesimal second-order stress tensor $\boldsymbol{\sigma}$ with a fourth-order tensor $\left(\boldsymbol{C}^{el}\right)^{-1}$ called the inverse elastic (i.e. stiffness) tensor [37,41,42]. The stiffness tensor has major and minor symmetry. For a given slip system with Burgers vector $\boldsymbol{b}$ and unit slip-plane normal $\hat{\boldsymbol{n}}$ in the crystal frame, the Orowan equation [43] is used and the second-order infinitesimal anelastic strain is

$$\epsilon^{an}(\boldsymbol{\sigma}) = \frac{N}{2}\frac{S(\boldsymbol{\sigma})}{V}\mathrm{Sym}(\boldsymbol{b}\otimes\hat{\boldsymbol{n}}), \tag{14}$$

where N/V is the number of FR sources with length L per unit volume V and $\mathrm{Sym}(\bullet)$ is the symmetric part of tensor $\bullet$. Hereby, slip is solely a function of the resolved shear stress.

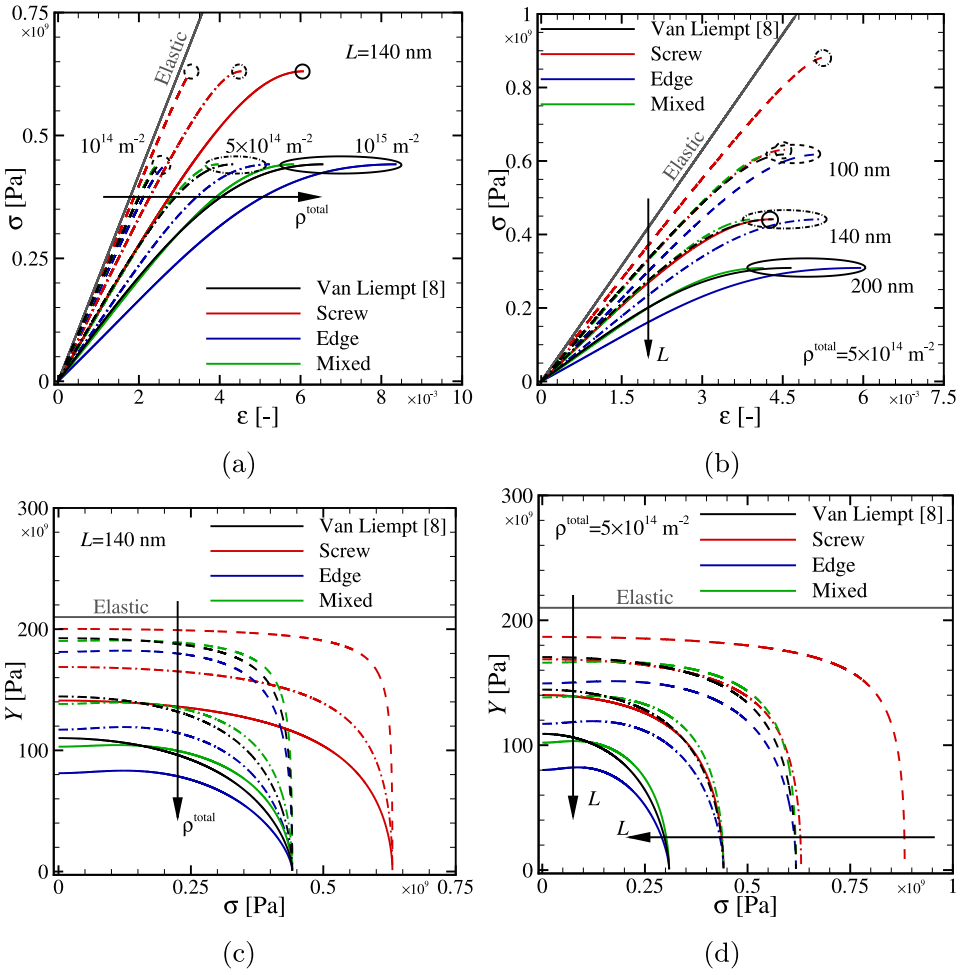

Fig. 6. The normal stress σ as a function of principal strain ϵ for (a) effective segment length $L = 140$ nm and total dislocation densities $\rho^{\text{total}} = 10^{14}$, 5×10^{14} and 10^{15} m^{-2}, and (b) density $\rho^{\text{total}} = 5 \times 10^{14}$ m^{-2} and lengths $L =$ 100, 140 and 200 nm. The tangent modulus Y as a function of the normal stress σ in (c) and (d). The arrows in (a) and (c) indicate an increase in total dislocation density ρ^{total}, and in (b) and (d) an increase in effective segment length L across lines with a given color.

For given stress tensor $\boldsymbol{\sigma} = \sigma \hat{\boldsymbol{d}} \otimes \hat{\boldsymbol{d}}$, where $\hat{\boldsymbol{d}}$ is a unit vector parallel to the normal stress with magnitude σ, the corresponding principal strain is $\epsilon = \boldsymbol{\epsilon} : \hat{\boldsymbol{d}} \otimes \hat{\boldsymbol{d}}$. The unit vector in the loading direction is

$$\hat{\mathbf{d}} = (\cos(\theta)\sin(\phi), \sin(\theta)\sin(\phi), \cos(\phi))^{\mathsf{T}}, \tag{15}$$

where θ is the azimuth angle, ϕ from here on the polar angle. The infinitesimal principal strain ϵ in the crystal frame is a superposition of the elastic and anelastic components ϵ^{el} and ϵ^{an}. The principal elastic lattice and anelastic strains are

$$\epsilon^{\text{el}}(\sigma, \hat{\boldsymbol{d}}) = \sigma \hat{\boldsymbol{d}} \otimes \hat{\boldsymbol{d}} : \left(\boldsymbol{C}^{\text{el}}\right)^{-1} : \hat{\boldsymbol{d}} \otimes \hat{\boldsymbol{d}} \tag{16a}$$

and

$$\epsilon^{\text{an}}(\sigma, \hat{\boldsymbol{d}}) = \hat{\boldsymbol{d}} \otimes \hat{\boldsymbol{d}} : \epsilon^{\text{an}}(\boldsymbol{\sigma}), \tag{16b}$$

respectively. In order to employ computational algebra to calculate the spatial representation of the moduli, the well-known Voigt scheme is used [40]. If the material is devoid of dislocations, the well-known definition of the linear elastic Young's modulus $E \equiv \sigma/\epsilon^{\text{el}}$ is obtained. Contrary, with dislocations present the tangent modulus $Y \equiv \partial\sigma/\partial\epsilon$ depends on the direction $\hat{\boldsymbol{d}}$, the magnitude of the normal stress σ and the dislocation structure. Furthermore, equation (16a) is not limited to isotropic or cubic elasticity but valid for any symmetric elastic tensor $\boldsymbol{C}^{\text{el}}$. We note that the effective Poisson's ratio is unaffected because volume is conserved during dislocation glide. Hence the scaled effective Poisson ratio $\nu(\theta, \phi)/\nu^{\text{el}}$ remains a unit sphere.

The scaled linear elastic Young's modulus $E(\theta, \phi)/E^{\text{el}}$ can be graphically represented in spherical coordinates $\{r, \theta, \phi\}$, with $r \equiv ||E(\theta, \phi)/E^{\text{el}}||$. For isotropic linear elastic materials devoid of dislocations [37,42], the Young's modulus is a unit sphere. Equivalent to the frequently used spherical representation of linear elastic anisotropy, the tangent modulus can be shown in spherical coordinates with $r \equiv ||Y(\sigma, \theta, \phi)/E^{\text{el}}||$. A two-dimensional representation by means of a stereographic projection onto the plane with its normal parallel to $\hat{\boldsymbol{e}}_3$ and containing the origin $\boldsymbol{o}$ is possible since $Y(\hat{\boldsymbol{d}}) = Y(-\hat{\boldsymbol{d}})$. The polar angle is expressed as $\phi = 2\tan^{-1}(r')$, with the polar coordinates $\{r', \theta\}$ [42]. The stereographic projection is included in Fig. 5.

4. Results

4.1. Isotropic mechanical response

In the following, we present the results for virtual tensile tests on polycrystalline materials. For an isotropic mechanical response, the principal strain is

$$\epsilon(\sigma) = \frac{\sigma}{E^{\text{el}}} + \epsilon^{\text{an}}(\sigma). \tag{17}$$

In Appendix B, the relation between the normal stress and resolved shear stress, and the principal anelastic strain and anelastic shear strain by the Taylor factor M [8,44,45] is revisited. Assuming FR sources to be uniformly distributed over $k = 12$ slip systems with dislocation density ρ^{slip} each, i.e. the total dislocation density $\rho^{\text{total}} = \sum_k \rho_k^{\text{slip}} \equiv k\rho^{\text{slip}}$, and substituting Eqs. (14) and (B.4) in Eq. (17), we give the total principal strain as

$$\epsilon(\sigma) = \frac{\sigma}{E^{\text{el}}} + \frac{b}{M}\left(\frac{\rho_{\text{e}}^{\text{total}} S_{\text{e}}(\sigma)}{L_{\text{e}}} + \frac{\rho_{\text{s}}^{\text{total}} S_{\text{s}}(\sigma)}{L_{\text{s}}}\right), \tag{18}$$

with $\rho^{\text{total}} \equiv \rho_{\text{s}}^{\text{total}} + \rho_{\text{e}}^{\text{total}}$, where $\rho_{\text{s}}^{\text{total}}$ and $\rho_{\text{e}}^{\text{total}}$, and L_{s} and L_{e} are the dislocation densities and effective segment lengths of screw and edge dislocations, respectively. In the works by Van Liempt and Sietsma [8] and Arechabaleta *et al.* [9,10], the equilibrium shape of the FR source is circular and the total principal strain is

$$\epsilon_{\text{iso}}(\sigma) \approx \frac{\sigma}{E^{\text{el}}} + \frac{M\rho^{\text{total}}\left(E^{\text{el}}\right)^2 b^3}{32(\nu+1)^2\sigma^2 L}\left(2\sin^{-1}\left(\frac{2(1+\nu)\sigma L}{ME^{\text{el}}b}\right) - \sin\left(2\sin^{-1}\left(\frac{2(1+\nu)\sigma L}{ME^{\text{el}}b}\right)\right)\right), \tag{19}$$

with L independent of dislocation character. Here, four cases are considered, namely: (1) the results by Van Liempt and Sietsma [8]; (2) only screw dislocation segments (i.e. $\rho_{\text{s}}^{\text{total}} = \rho^{\text{total}}$ and $\rho_{\text{e}}^{\text{total}} = 0$) with length $L_{\text{s}} = L$; (3) only edge dislocation segments (i.e. $\rho_{\text{s}}^{\text{total}} = 0$ and $\rho_{\text{e}}^{\text{total}} = \rho^{\text{total}}$) with length $L_{\text{e}} = L$; (4) mixed dislocation densities $\rho_{\text{s}}^{\text{total}} = \rho_{\text{e}}^{\text{total}} = \rho^{\text{total}}/2$ with lengths $L_{\text{e}} = L_{\text{s}} = L$. First, the total dislocation density $\rho^{\text{total}} = 10^{14},\ 5\times10^{14}$ and 10^{15} m^{-2} is varied while the effective segment length $L = 140$ nm is kept constant; secondly, the effective segment length $L = 100$, 140 and 200 nm changes while the total dislocation density $\rho^{\text{total}} = 5\times10^{14}$ m^{-2} remains constant. In Fig. 6, the tensile results are presented with Young's modulus $E^{\text{el}} = 210\times10^9$ Pa, Poisson's ratio $\nu = 0.3$, Taylor factor $M = 3.06$ [46–48] and Burgers vector magnitude $b = 0.25$ nm. In Fig. 6, the elastic response is represented by a solid gray line marked "Elastic". The results with constant effective segment length $L = 140$ nm and total dislocation densities $\rho^{\text{total}} = 10^{14}, 5\times10^{14}$ and 10^{15} m^{-2} are indicated by dashed, dash-dotted and solid lines, respectively. The same line patterns hold for results with constant density $\rho^{\text{total}} = 5\times10^{14}$ m^{-2} and lengths $L =$ 100, 140 and 200 nm.

While varying the total dislocation density for the effective segment length $L = 140$ nm, we observe in Fig. 6a that the principal strain increases with dislocation density. The principal anelastic strain is the horizontal distance between the line $\sigma \equiv E^{\text{el}}\epsilon$ and any point on the tensile curve. When the dislocation density per slip plane is increased, and in turn, so is the anelastic dislocation strain (See Eq. 14). In Fig. 6b, the dislocation density $\rho^{\text{total}} = 5\times10^{14}$ m^{-2} and the effective segment length is varied. We observe that the principal anelastic strain increases with effective increasing segment length. The anelastic dislocation shear strain scales with the area swept by an FR source, which scales with the square of the effective segment length, $S \propto L^2$. Furthermore, the normal stress for a given anelastic strain is inversely proportional to the effective segment length because the self-stress scales with the curvature of the bowed-out dislocation. In the present work dissipation is not accounted for, hence why the initial modulus deviates from the isotropic linear elastic modulus from the start of loading. Furthermore, the tangent modulus vanishes when the applied stress matches the line tension, because upon further expansion of the FR loops the line stress decreases.

The differences between the prediction by Van Liempt and Sietsma [8] and the results for solely screw or edge dislocations are striking. Between screw dislocations and the prediction by [8], the normal stress for a given total principal strain differ up to a factor $1/(1-\nu)$, i.e. on the order of 50%. Also for a given stress the principal anelastic strains differ up to a factor $(1-\nu)$. Hence the normal stress is underestimated and total principal strain overestimated. While the range of normal stresses is unaffected between edge dislocations and the prediction by [8], the anelastic dislocation strains differ a factor $1/(1-\nu)$, hence the total principal strain is underestimated. The observed differences are easily rationalized by considering an elliptical equilibrium shape and with the results in 4 for initial screw and edge character sources. The prediction by [8] and the results for mixed dislocation segments match closely.

In order to present the tangent modulus, we take the inverse of the derivative of Eq. (19) with respect to the normal stress and obtain the isotropic tangent modulus [8], i.e.

$$Y_{\text{iso}}(\sigma) \approx \left(\frac{1}{E^{\text{el}}} + \frac{\rho^{\text{total}}Lb}{2M\sigma}\frac{\left(ME^{\text{el}}b\right)^2}{(2(\nu+1)\sigma L)^2}\left(\sqrt{\frac{(2(\nu+1)\sigma L)^2}{\left(ME^{\text{el}}b\right)^2 - (2(\nu+1)\sigma L)^2}} - \sin^{-1}\left(\frac{2(\nu+1)\sigma L}{ME^{\text{el}}b}\right)\right)\right)^{-1}. \tag{20}$$

In Figs. 6c and 6d the tangent modulus as a function of the normal stress (extended Kocks-Mecking plot [8]) is presented. These correspond to Figs. 6a and 6b, respectively. In Fig. 6c, we observe that the initial modulus decreases with increasing total dislocation density. Furthermore, in Fig. 6d, the given change in segment length affects the initial moduli. The inverse relationship between the yield stress and the effective segment length is clearly visible in Fig. 6d. Considering the prediction by Van Liempt and Sietsma [8] and the results for mixed dislocation segments, we observe that the tangent moduli are close as well.

Arechabaleta *et al.* [9] evaluated the validity of the model with approximate circular equilibrium shape [8] by comparison with dislocation densities from X-Ray Diffraction (XRD) measurements. The dislocation densities $10^{12} < \rho^{\text{total}} \leq 10^{14}$ m^{-2} obtained through aforementioned model [8] were consistent with those obtained by XRD. We note that the prediction by [8] approximates the results for isopycnic dislocation densities in Fig. 6. Isopycnic means of, relating to, or marked by equal or constant density. Hereby, the experimental XRD diffraction and tensile-test measurements of the total dislocation density ρ^{total} might have agreed too.

It is of interest to study the effect of different screw and edge dislocations densities on previously experimentally obtained total dislocation densities and effective segment lengths. They were calculated by means of Eqs. (19) and (20) [8–10]. Here, a set of virtual tensile tests is performed for various edge and screw dislocation densities $\rho_{\text{s}}^{\text{total}}/\rho^{\text{total}} = 1 - \rho_{\text{e}}^{\text{total}}/\rho^{\text{total}} = 0$, 1/8, 1/4, 3/8, 1/2, 5/8, 3/4, 7/8, 15/16, 99/100 and 1. In Fig. 7, the tensile results are given by solid black lines with screw dislocation densities $\rho_{\text{s}}^{\text{total}}/\rho^{\text{total}} = 0,\ 1/2,\ 3/4$ and 1, total dislocation density $\rho^{\text{total}} = 10^{15}$ m^{-2} and effective segment length $L = 140$ nm. Here the dashed gray line marked "Elastic" indicates the linear elastic response; in Fig. 7b, the tangent modulus as a function of the normal stress is given. Subsequently, a non-linear fitting and the fitting procedure as followed by Van Liempt and Sietsma [8] are preformed on the tensile-test data sets. The former method is the damped least-squares (DLS) method [49,50] with Eq. (19), $L = L_{\text{iso}}$ and $\rho^{\text{total}} = \rho_{\text{iso}}^{\text{total}}$. In the latter method, the effective segment length L_{iso} is obtained at the yield points with critical normal stress $\sigma_{\text{c}} \equiv M\mu^{\text{el}}b/L_{\text{iso}}$; the initial Young's modulus, i.e. $E \equiv \lim_{\sigma\to0} Y(\sigma)$, is used to determine the effective dislocation density $\rho_{\text{iso}}^{\text{total}}$. The numerical fits by DSL method and the method by Van Liempt and Sietsma are indicated by solid blue and dashed red lines, respectively, in Figs. 7a and 7b solely for $\rho_{\text{s}}^{\text{total}}/\rho^{\text{total}} = 0,\ 1/2,\ 3/4$ and 1. In Fig. 7c, the obtained ratios L_{iso}/L and $\rho_{\text{iso}}^{\text{total}}/\rho^{\text{total}}$ are presented. The red triangle and blue gradient symbols in Figs. 7a and 7b indicate results of the DLS method and the method by Van Liempt and Sietsma [8], respectively. The symbols in Fig. 7c correspond to the tensile-test data with varying screw dislocation density $\rho_{\text{s}}^{\text{total}}$. The (dashed) lines connecting these symbols are guides to the eye. The results for solely screw dislocations are indicated separately. They represent a limit case given the difference in yield strength from finite edge dislocation densities. The goodness of fit is assessed by calculating the coefficient of determination R^2. The obtained coefficients of determination are between $R^2 = 0.96$ and 1. The non-linear fits by DLS method for ratio $3/4 \leq \rho_{\text{s}}^{\text{total}}/\rho^{\text{total}} < 1$ do not converge to the global minimum and are therefore omitted.

The effective dislocation density $\rho_{\text{iso}}^{\text{total}}$ is significantly affected by the ratio between edge and screw dislocations. In the limit of solely edge dislocations, the total dislocation density ρ^{total} is overestimated. The observed effective segment length L_{iso} differs far less from the actual length L because the yield strength $\sigma_{\text{c}} \propto 1/L$. For an approximately

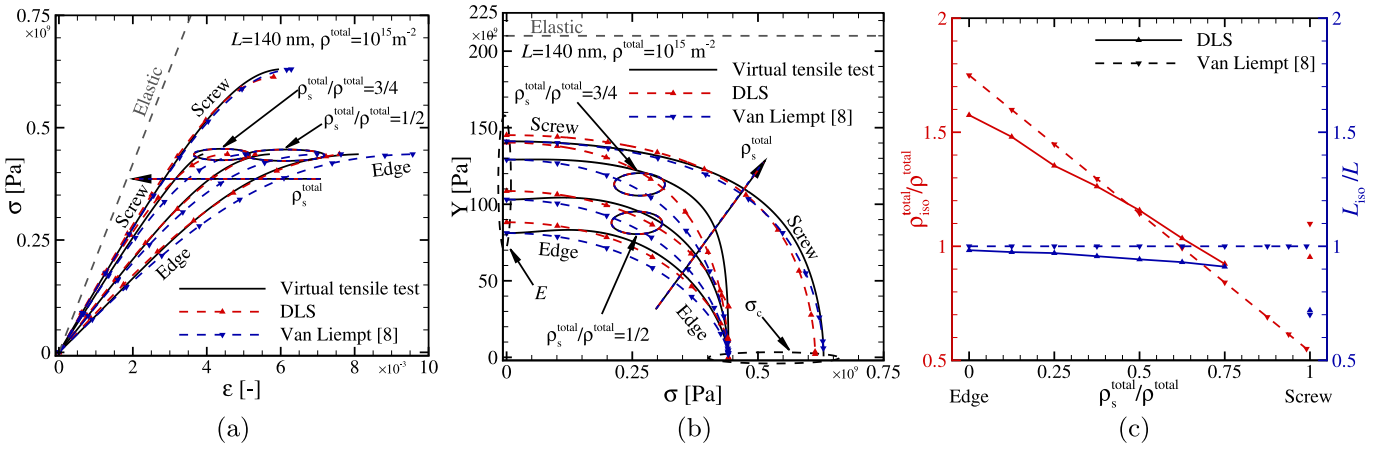

Fig. 7. (a) The normal stress σ as a function of the principal strain ϵ and (b) the tangent modulus Y as a function of the normal stress σ with screw dislocation densities $\rho_s^{\text{total}}/\rho^{\text{total}} = 0,\ 1/2,\ 3/4$ and 1, total density $\rho^{\text{total}} = 10^{15}$ m^{-2} and effective segment length $L = 140$ nm. The arrows in (a) and (b) indicate an increase in total screw dislocation density ρ_s^{total} across equivalently coloured lines. (c) The ratios $\rho_{\text{iso}}^{\text{total}}/\rho^{\text{total}}$ and L_{iso}/L as a function of the scaled screw dislocation density $\rho_s^{\text{total}}/\rho^{\text{total}}$ via the damped least-squares (DLS) method and the method by Van Liempt and Sietsma [8].

elliptic dislocation loop, the observed total dislocation density $\rho_{\text{iso}}^{\text{total}}$ and segment length L_{iso} agree well with density ρ^{total} and length L when the ratio $\rho_s^{\text{total}}/\rho^{\text{total}} \approx 1/(2-\nu)$. For Poisson's ratio $\nu = 1/3$ this screw dislocation density $\rho_s^{\text{total}}/\rho^{\text{total}} \approx 0.58$ and in agreement with the observed unit ratios between $\rho_s^{\text{total}}/\rho^{\text{total}} \approx 0.62 - 0.64$. The method by Van Liempt and Sietsma underestimates the total dislocation density ρ^{total} for a majority of screw dislocations, i.e. $1/2 << \rho_s^{\text{total}}/\rho^{\text{total}} < 1$. Finally, for solely screw dislocations, the effective segment length is underestimated by a factor ~ 0.3 because the critical shear stress is $\tau_c/(1-\nu)$. The effective dislocation density $\rho_{\text{iso}}^{\text{total}}$ differs marginally from the given total density ρ^{total}. This is non-trivial. Quantifying the observational error in previous works is however only possible if additional information on the geometry of the given dislocation network was measured. The method here does not need additional observations on the dislocation network geometry. The orientation of individual dislocations and a generic Poisson's ratio are *a priori* incorporated.

4.2. Anisotropic mechanical response

In the following, we present the results for virtual tensile tests on single crystallites with cubic crystal lattices. In the supplementary material [40], the slip systems in face- and body-centred (FCC and BCC) crystallites, respectively, are given. For BCC crystallites, only twelve $\langle 111\rangle\{110\}$ slip systems are considered. They form the six main glide planes at low temperatures [28], instead of the forty-eight potential slip systems which include $\{112\}$ and $\{123\}$ planes. In order to present the effect of a nonuniform dislocation distribution, the effective segment length $L_s = L_e = L$ is kept constant and solely the coefficient ρ^{slip} is varied. The present method is not limited to the same fractions of initial dislocation segments with a given character per slip-system either. Though under static loading conditions it remains necessary to use effective segment lengths which characterize the ensemble of dislocations in a given crystallite.

Dislocations are spread homogeneously across each active slip-system contained within a single crystallite. The total dislocation density per slip system $\rho^{\text{slip}} \equiv \rho_s^{\text{slip}} + \rho_e^{\text{slip}}$, where ρ_s^{slip} and ρ_e^{slip} are the screw and edge dislocation densities per slip system. We choose to limit the results to pure (or a mixture of pure) screw and edge character segments. The present method is not limited to these assumptions, but needs numerical root-finding to approximate the equilibrium solution for an arbitrary initial dislocation character ($\phi_i \neq -\pi/2,\ 0,\ \pi/2$ and π) for Poisson's ratio $\nu \neq 0$, while the closed-form expressions for initial pure edge and screw character segments do not. The dislocation density on each glide plane is defined as the sum of its constituent slip systems. Here, we use the seminal proportionality coefficient $\alpha \equiv \left(L\sqrt{\rho^{\text{total}}}\right)^{-1} = 1/3$ which was both experimentally [10] ($\alpha \approx 0.4$) and theoretically [51] obtained.

In order to validate our method with the works by Koehler and DeWit [6], and Agrawal and Verma [7], we take the series expansion of Eq. (13a) around zero applied shear stress and obtain the engineering shear strain

$$\gamma_{xz}^{\text{an}} = \frac{b\rho^{\text{slip}}}{L} S(\tau_{xz}) \simeq \frac{\rho^{\text{slip}} L^2}{6} \frac{\tau_{xz}}{\mu^{\text{el}}}. \tag{21}$$

Assuming the dislocation density ρ^{slip} to be constant across all slip systems and Poisson's ratio $\nu = 0$, we give the fourth-order inverse anelastic tensor in vector-matrix notation as

$$\begin{pmatrix} \epsilon_{11}^{\text{an}} \\ \epsilon_{22}^{\text{an}} \\ \epsilon_{33}^{\text{an}} \\ 2\epsilon_{23}^{\text{an}} \\ 2\epsilon_{13}^{\text{an}} \\ 2\epsilon_{12}^{\text{an}} \end{pmatrix} \simeq \frac{\rho^{\text{slip}} L^2}{12\mu^{\text{el}}} \begin{pmatrix} \frac{8}{3} & -\frac{4}{3} & -\frac{4}{3} & 0 & 0 & 0 \\ -\frac{4}{3} & \frac{8}{3} & -\frac{4}{3} & 0 & 0 & 0 \\ -\frac{4}{3} & -\frac{4}{3} & \frac{8}{3} & 0 & 0 & 0 \\ 0 & 0 & 0 & \frac{8}{3} & 0 & 0 \\ 0 & 0 & 0 & 0 & \frac{8}{3} & 0 \\ 0 & 0 & 0 & 0 & 0 & \frac{8}{3} \end{pmatrix} \cdot \begin{pmatrix} \sigma_{11} \\ \sigma_{22} \\ \sigma_{33} \\ \sigma_{23} \\ \sigma_{13} \\ \sigma_{12} \end{pmatrix}. \tag{22}$$

This corresponds to the results for a uniform distribution of dislocations across all glide planes in FCC by Koehler and DeWit [6] and in BCC by Agrawal and Verma [7].

For a single active glide plane with two active slip systems in FCC and BCC, we find Tetragonal *versus* Rhombic anisotropic symmetry because of the difference in angles between the Burgers vectors $\langle 110\rangle/2$ and $\langle 111\rangle/2$. Inactive slip systems and/or glide planes are devoid of dislocations and active ones have isopycnic dislocation densities. For two active glide planes Rhombic *versus* Tetragonal anisotropic symmetry is found. In addition the angles between glide plane normals, $\{111\}/\sqrt{3}$ and $\{110\}/\sqrt{2}$, differ. The anisotropic symmetry is unique for any (non)uniform distribution of dislocations and depends on the crystal structure as well. Furthermore, the obtained anisotropic symmetry is independent of Poisson's ratio ν and a given normal stress below the yield stress. We find it notable that for distributions with differing edge and screw dislocation densities the number of symmetry planes reduces. The anisotropic ratio [52] and index [53] do depend on dislocation distribution, densities and characters. In the supplementary material [40], the normalised initial Young's moduli E/E^{el} for nonuniform distributions of dislocations in FCC and BCC are presented. Finally, as expected

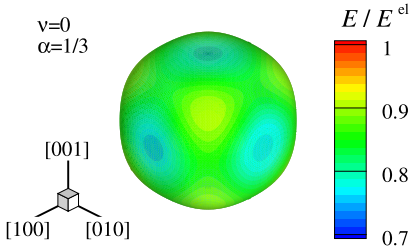

Fig. 8. The normalised initial Young's modulus E/E^{el} in spherical coordinates for a cubic crystallite with Poisson's ratio $\nu = 0$ and a uniform distribution of dislocations across all glide planes.

for the uniform distribution of dislocations across all glide planes, the initial modulus has cubic anisotropy as seen in Fig. 8.

4.3. Limit analysis

In the following, we consider the compressibility and incompressibility limits, i.e. Poisson's ratios $\nu = 0$ and $1/2$. In the supplementary material [40], the normal stress-strain relations are presented in five rational tensile directions for several nonuniform dislocation distributions in FCC and BCC. For tensile tests on single crystallites, it is well-known that the normal stress at yield is predicted by means of the Schmid factor and the often used critical shear stress $\tau_c \equiv \mu^{el} b/L$ [54]. Hence the yield stress decreases, or remains the same, as more glide planes become active. The normal stress-strain relationships for a uniform distribution of dislocations are the same for FCC and BCC. From here on, only cubic lattices with uniform dislocation distributions are considered.

In Fig. 9, the tensile results are presented with Poisson's ratio $\nu = 1/2$, edge or screw dislocations and rational tensile directions $\langle 100\rangle$, $\langle 110\rangle$ and $\langle 111\rangle$. In Fig. 9, the rational tensile directions are indicated by coloured dots on the inserted stereographic projection of Fig. 8. The stress σ_c and strain ϵ_c at yield are depicted by coloured triangle and gradient symbols in Fig. 9. Note that the choice of normalization originates from $E^{el}/2 \equiv \mu^{el}$ for Poisson's ratio $\nu = 0$. It is obvious that the strain ϵ is not obtained by the linear elastic stiffness alone because FR sources contribute significantly to the total principal strain. As expected, we obtain the largest anelastic dislocation strain contribution for edge character segments and Poisson's ratio $\nu = 1/2$. Intermediate values are found for Poisson's ratio $\nu = 0$ independent of initial dislocation character (See Fig. 10) and the smallest anelastic strain contribution results for screw dislocations and Poisson's ratio $\nu = 1/2$. The anisotropy is not affected by the dislocation character.

In Figs. 9b and 9c, the normalised tangent moduli Y/E^{el} as a function of the normalised stress $2\sigma L/(E^{el}b)$, and the normalised strain $2\epsilon L/b$, respectively, are presented. The flow-stress σ_c and critical principal strain ϵ_c are the intersects of given tangent modulus with $Y/E^{el} = 0$. During tensile experiments the observed tangent modulus does not reduce to zero for critical normal stress σ_c [8–10,55,56]. Before the tensile curve becomes horizontal, work-hardening initiates with shear stress contribution τ_w and plastic shear strain γ_p. The flow stress is $\sigma_f \simeq \sigma_c + \sigma_w$ and the work-hardening gradient $\Theta \equiv \partial\sigma_f/\partial\epsilon_p$. Values of constant gradient Θ during Stage-I/II/III work-hardening are typically one to three orders of magnitude smaller than the elastic Young's modulus [1]. Hence plastic deformation commences when the tangent modulus, Y, equals the work-hardening gradient, Θ. Moreover, the critical stress σ_c and strain ϵ_c are the upper bounds of the yield point.

In Fig. 9, we observe a marked difference between the tangent moduli for edge or screw dislocation segments. Regarding initial edge character segments in the limit $\sigma \to 0$, we find that the initial tangent modulus approaches zero. This is readily understood by taking the limit $\lim_{\tau_{xz}\to 0} \partial\Delta\phi_e/\partial\tau_{xz}$ of Eq. (12b). It is intuitive that with a given change of dislocation character at both pinning points, the total dislocation line length either increases or decreases, and the local line sense changes. The associated change in potential energy can be split into: (1) a contribution solely due to line length change with constant dislocation character; and (2), a change in self-energy with dislocation character for a constant line length. Even though the line length increases when a given FR source with initial pure edge character bows out, the increase in potential energy associated with total segment length is lowered because dislocation character changes along the dislocation loop. From pure edge character, which has the maximum self-energy for a finite Poisson's ratio, the local line sense changes to a mixed character. In the limit of an incompressible solid, the total energy change is zero because the increase in potential energy per unit dislocation line length with constant character equals the reduction in self-energy with dislocation character. Contrarily, when a given FR source with initial pure screw character bows out, the potential energy increases with both dislocation line length and the change of character. Hence the apparent elastic constants depend on the initial dislocation character and compressibility.

It is of interest to compare our results with the isotropic predictions by Van Liempt and Sietsma [8]. Moreover, a mix of initial edge and screw characters segments is incorporated. In Fig. 10, the tensile results are presented with Poisson's ratios $\nu = 0$ and $1/2$, and isopycnic dislocation densities. In Fig. 10a, the normal stress-strain relation is given and the isotropic results for Taylor factor $M = 3.06$ are represented with dashed and solid black lines. The

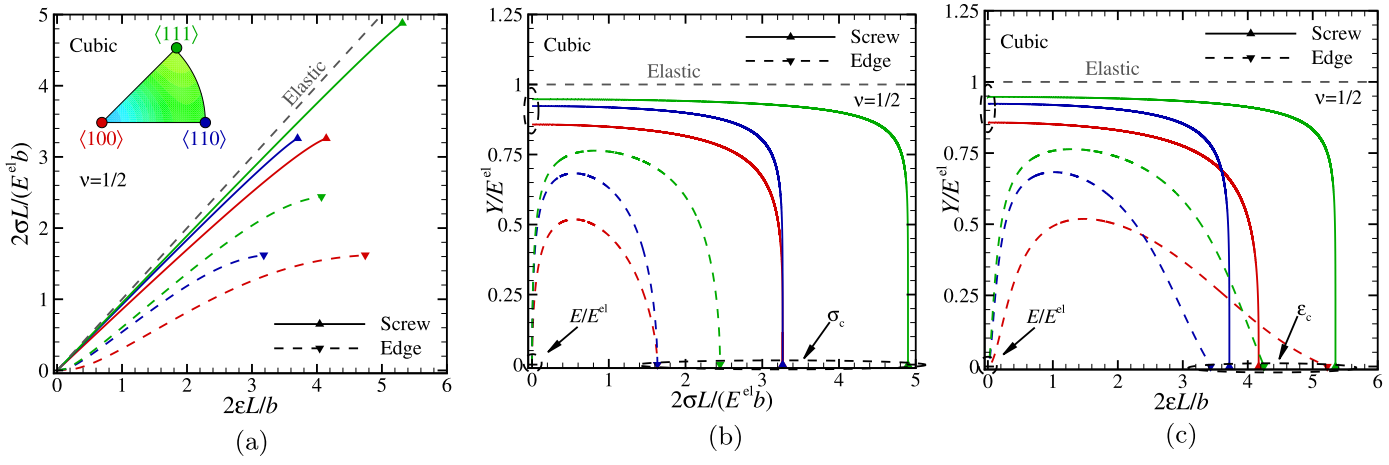

Fig. 9. (a) The normalised normal stress $2\sigma L/(E^{el}b)$ as a function of normalised principal strain $2\epsilon L/b$, (b) the normalised tangent modulus Y/E^{el} as a function of the normalised stress $2\sigma L/(E^{el}b)$, and (c) the normalised strain $2\epsilon L/b$ with Poisson's ratio $\nu = 1/2$ in rational tensile directions $\langle 100\rangle$, $\langle 110\rangle$ and $\langle 111\rangle$.

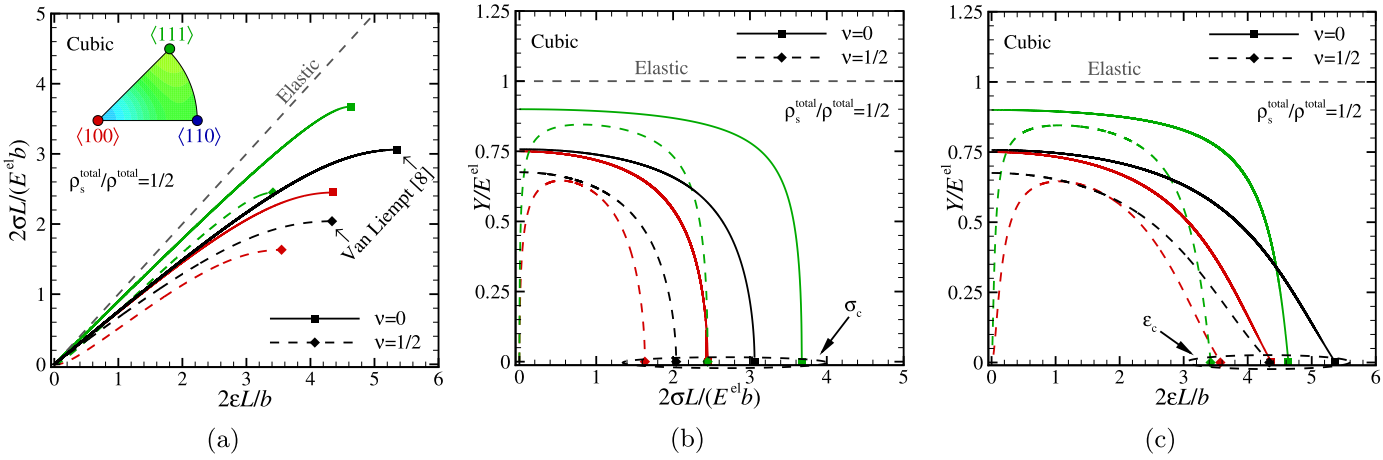

Fig. 10. (a) The normalised normal stress $2\sigma L/(E^{el}b)$ as a function of normalised principal strain $2\varepsilon L/b$ with Poisson's ratios $\nu = 0$ and 1/2, screw dislocation density $\rho_s^{total}/\rho^{total} = 1/2$ and rational tensile directions ⟨100⟩ and ⟨111⟩. The normalised tangent modulus Y/E^{el} as a function of (b) the normalised stress $2\sigma L/(E^{el}b)$ and (c) the normalised strain $2\varepsilon L/b$. The dashed and solid black lines indicate the isotopic results in (19) and (20) by Van Liempt and Sietsma [8].

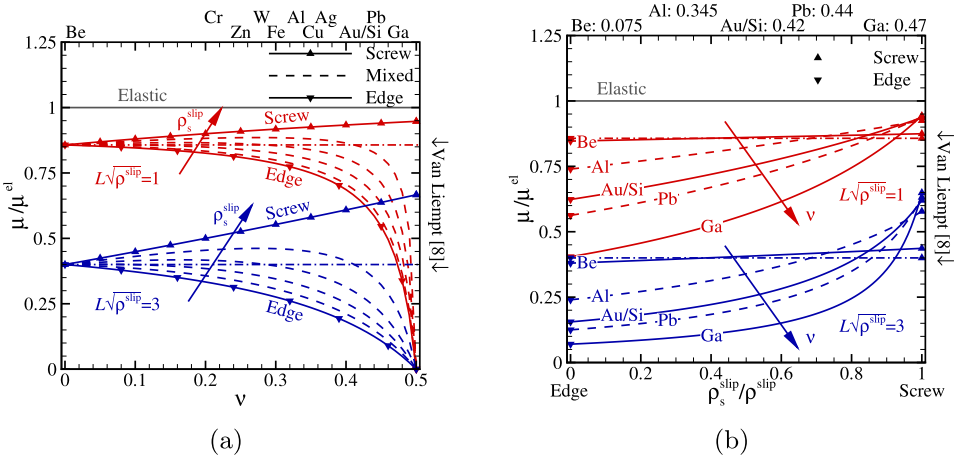

Fig. 11. The normalised initial shear modulus μ/μ^{el} as a function of (a) the Poisson's ratio ν and (b) the scaled screw dislocation density $\rho_s^{slip}/\rho^{slip}$ with inverse coefficients $L\sqrt{\rho^{slip}} = 1$ and 3. The arrows indicate an increase in (a) screw dislocation density ρ_s^{slip} and (b) Poisson's ratio ν across equivalently coloured lines.

solid and dashed lines correspond to Poisson's ratios $\nu = 0$ and 1/2, respectively. Comparing Figs. 9a and 10a for Poisson's ratio $\nu = 1/2$, we observe that the yield stress is determined by the initial edge dislocation segments. These segments attain their critical shape before initial screw segments as predicted by Kovacs [27]. The principal strain for a given stress decreases compared to solely edge dislocations since $\rho_e^{total} < \rho^{total}$ (See Figs. 9 and 10). The predicted critical normal stress σ_c by Van Liempt and Sietsma [8] agrees well with single crystallite results because the critical shear stress is $\tau_e^c \equiv \mu^{el}b/L$. However, the predicted total principal strain at yield ϵ_c by Van Liempt and Sietsma [8] is an overestimate because the anelastic shear strain across different slip systems is the same (See Appendix B). Contrarily, here the anelastic shear strain depends on slip system orientation. Hence not every slip system contributes equally in the given tensile direction. The exaggerated anelastic strain in the isotropic model [8] leads to overestimating the total dislocation density (See Section 4.1).

The cubic tangent moduli and the isotropic tangent modulus by Van Liempt and Sietsma [8] are given in Figs. 10b and 10c. The Taylor factor M proportionally scales the isotropic curves. For Poisson's ratio $\nu = 0$, the functional forms of our results and the isotropic prediction by [8] agree. For Poisson's ratio $\nu = 1/2$, we observe a large disparity between our results and the isotropic tangent modulus by [8]. Notable are the differences in tangent moduli for small normal stresses and principal strains. This is readily understood because the self-energy in the isotropic prediction by Van Liempt and Sietsma [8] is independent of dislocation character. Hereby, the potential energy always increases with dislocation line length. Hence the gradient of the normal stress/strain-to-modulus relation is negative for any normal stress (and principal strain).

In order to illustrate the effects of compressibility, ν, and dislocation densities ρ_s^{total} and ρ_e^{total}, the normalised initial shear modulus, $\mu/\mu^{el} \equiv \lim_{\tau_{xz}\to 0} \mu(\tau_{xz})/\mu^{el}$, is given as a function of the Poisson's ratio ν and density $\rho_s^{slip}/\rho^{slip}$ in Fig. 11. The densities are varied from solely edge to only screw dislocations in increments of $\Delta\rho_s^{slip} = \rho^{slip}/5$ across coloured (dashed) lines in Fig. 11a. The shear moduli are presented for the given proportionality coefficients $(L\sqrt{\rho^{slip}})^{-1} = 1/3$ and 1 in a single active slip system. Several metals are depicted in Fig. 11a with their horizontal loci corresponding to their respective Poisson's ratios, e.g. Au and Si with $\nu = 0.42$, and Cr with $\nu = 0.21$. The initial shear moduli predicted by Van Liempt and Sietsma [8] are depicted by horizontal dashed-dotted lines. The initial modulus as a function of the screw dislocation density is given in Fig. 11b, for several Poisson's ratios. As expected, we observe that the initial modulus is only independent of dislocation character for Poisson's ratio $\nu = 0$. Otherwise, when a given FR source with initial pure screw character bows out, the potential energy increases with dislocation line length and the change of local line sense towards a mixed character. Hereby, the initial shear modulus increases with Poisson's ratio ν and screw dislocation density ρ_s^{slip}. Juxtaposed, the increase in potential energy with line length is lowered because of the

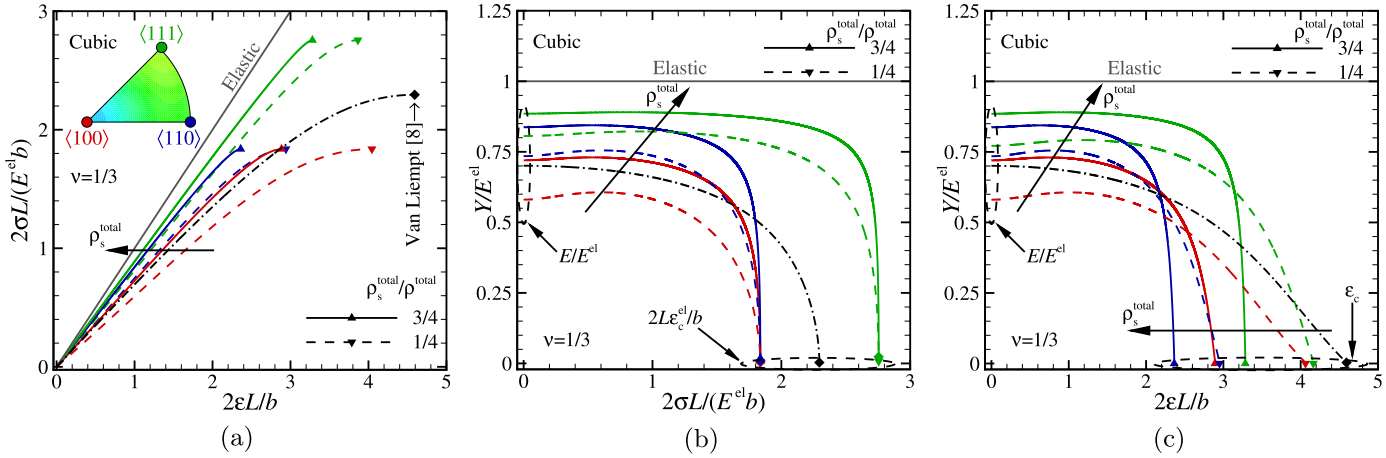

Fig. 12. (a) The normalised normal stress $2\sigma L/(E^{\mathrm{el}}b)$ as a function of normalised principal strain $2\epsilon L/b$ with densities $\rho_{\mathrm{s}}^{\mathrm{total}}/\rho^{\mathrm{total}} = 1/4$ and $3/4$, and rational tensile directions ⟨100⟩, ⟨110⟩ and ⟨111⟩. The normalised tangent modulus Y/E^{el} as a function of (b) the normalised stress $2\sigma L/(E^{\mathrm{el}}b)$ and (c) the normalised strain $2\epsilon L/b$. The black arrows marked with $\rho_{\mathrm{s}}^{\mathrm{total}}$ indicate an increase in screw dislocation density $\rho_{\mathrm{s}}^{\mathrm{total}}$ across lines with a given color. The dashed-dotted black line indicates the isotopic results in (19) and (20) by Van Liempt and Sietsma [8].

formation of mixed character dislocation line from an initial pure edge dislocation. Hence the initial modulus depends on the fractions of screw and edge dislocations. For a given increase in Poisson's ratio $\nu \geq 0.4$ and/or edge dislocation density $\rho_{\mathrm{e}}^{\mathrm{slip}}$, the initial shear modulus tends to zero. As expected, the initial modulus decreases with increasing coefficient $L\sqrt{\rho^{\mathrm{slip}}}$. A given decrease in proportionality coefficient α implies an increase in dislocation density and/or initial segment length. Apart from an increase in dislocation density after plastic deformation, the accompanying changes in dislocation character affect the initial moduli. This might explain why accurate predictions of the apparent linear elastic constants after plastic deformation proved impossible up to now [9].

4.4. Cubic crystallites

In the following, we study materials with Poisson's ratio $\nu = 1/3$ which is commonly used for steels and aluminum. It is well-known that at low temperatures BCC iron contains predominantly screw dislocations [57]. Furthermore, BCC related non-Schmid effects [58], e.g. the lack of mirror symmetry with respect to planes orthogonal to the dominant ⟨111⟩ slip directions and the structure of the screw cores, are not considered here. Recently, Cash and Cai [14] discussed the surplus of edge dislocations in fatigued FCC metals. Given that a dislocation network is continuous and cannot terminate inside the bulk, a single character segment distribution is rare. Here, dislocation densities $\rho_{\mathrm{s}}^{\mathrm{total}}/\rho^{\mathrm{total}} = 1/4$ and $3/4$ are considered. The virtual tensile results are presented in Fig. 12. As expected [27], the yield strength is independent of screw dislocation density $\rho_{\mathrm{s}}^{\mathrm{total}}$. Here, the initial segment lengths are equal $L_{\mathrm{s}} = L_{\mathrm{e}}$. Thus edge character FR sources become critical first; when $L_{\mathrm{s}} > L_{\mathrm{e}}/(1-\nu)$, screw character FR sources become critical before edge character segments. Hence the yield strength depends on the length of edge character segments, or the segment length of screw dislocations. This is a general observation. The isotropic prediction by Van Liempt and Sietsma [8] with Taylor factor $M = 3.06$ is indicated by a dashed-dotted black line with diamond symbols in Fig. 12. In accordance with Fig. 11, the initial Young's modulus E/E^{el} increases with increasing screw dislocation density $\rho_{\mathrm{s}}^{\mathrm{total}}$. We note that the gradients of the cubic tangent moduli Y/E^{el} are initially positive. The positive initial gradient is markedly different from the prediction by Van Liempt and Sietsma [8]. The principal strain increases with edge dislocation density $\rho_{\mathrm{e}}^{\mathrm{total}}$. The increase in anelastic strain is most apparent at the yield stress (See Figs. 12b and 12c). Given that the anelastic strain increases with (edge) dislocation density, the linear elastic stiffness cannot *a priori* predict the principal strain in compressible materials either.

In order to experimentally obtain information on a physical dislocation network, the quantitative and qualitative change in stress-strain relationship, with a given change in dislocation densities, has to be observable. It is obvious that this criterion is satisfied for Poisson's ratio $\nu = 1/2$ (See Figs. 9–11). However, many engineering materials are compressible due to which the difference in initial moduli decreases (See Fig. 11). Fortunately, the anelastic strain, and in turn the tangent moduli, differ significantly for Poisson's ratio $\nu = 1/3$. This is most apparent between the tensile results in the ⟨100⟩ directions. These display a difference in initial moduli E of about a tenth of the linear elastic Young's modulus E^{el}; the difference in principal strains ϵ_{c} is about half the elastic strain $\epsilon_{\mathrm{c}}^{\mathrm{el}}$ for σ_{c} (See Fig. 12b). The latter is intuitive because an initial edge character FR source sweeps out a large area S near activation of the FR source.

Nearly all crystals are elastically anisotropic, at least to some extent. For several technically important engineering materials with cubic anisotropy the Zener ratio $Z \equiv 2C_{44}/(C_{11} - C_{12})$ [59]. In materials with low Zener ratios, the FR source equilibrium shape is approximately elliptical because self-energy chiefly depends on dislocation character. As the anisotropy ratio increases, discrete segments of the dislocation loop tend to align themselves along directions which are not necessarily screw orientations. Even so, Fitzgerald [33] showed that the critical shear stress τ_{xz}^{c} of various initial dislocation segment orientations, in BCC iron at room temperature, is approximated within an order of magnitude by an equivalent elastically isotropic material provided that $Z < 5$. When the ratio $Z \geq 2.5$, depending on the Burgers vector and slip system, sharp corners emerge in the dislocation loop equilibrium shape. Contrary to the elastically isotropic case, these corners are not directly associable with dislocation character [33]. Those sharp corners are due to thermodynamic instability of certain dislocation orientations [35] as a given crystallite's anisotropy ratio increases with, e.g., temperature. The influences of Zener ratio and dislocation orientation in α-iron are comprehensively discussed in [33–36].

Firstly, we argue that aluminum is a promising candidate to perform single crystal tensile-test upon. Foremost, aluminum is considered a "fairly isotropic" FCC material with anisotropy ratio 1.23 (equal to the Zener ratio for cubic anisotropy [52]). The Poisson's ratio $\nu \approx 0.33$ is high enough to experimentally obtain distinguishable changes in tangent modulus and yield point with a given change in dislocation density, effective segment length and dislocation character. Furthermore, the emergence of a surplus of edge character dislocation segment is expected for a fatigued specimen [14]. This warrants a noticeable change in tensile behaviour. Secondly, for crystallites with cubic anisotropic elasticity, Scattergood and Bacon [32] developed a method to calcu-

late effective elastic isotropic moduli with dislocations in mind. Note that these effective elastic isotropic moduli are not the apparent elastic moduli, but similar to the Voigt [60] and Reuss [61] average elastic moduli, which were developed to model the aggregate behaviour of poly-crystallites. The effective moduli are defined as explicit functions of the pre-logarithmic part of the self-energy of straight screw and edge dislocations in a given slip system. Aubry *et al.* [35] showed that one can model dislocation loop equilibrium shapes in BCC crystallites using the isotropic elasticity and Scattergood and Bacon's approximation. According to [35], the Scattergood and Bacon model produces results in reasonable agreement with the full anisotropic numerical calculations of a given dislocation loops on a given slip system. Our framework distinguishes between different slip systems and allows for tailoring the effective elastic constants per glide plane, and even per initial line sense and Burgers vector. This allows one to model the tangent moduli and yield points in crystallites with high Zener ratios, e.g, in single iron crystallites with $Z \approx 8$ as the α-γ transition is approached [62]. The present elastic-anelastic constitutive model takes account of anisotropic effects on a per-grain basis. For crystallographically textured materials, with e.g. cubic elasticity, an additional level of abstraction is necessary beyond the present constitutive model, which is satisfied by probabilistic or spatially resolved crystal plasticity methods.

5. Concluding remarks

In this work, the anisotropic tangent moduli and the yield points for heterogeneous dislocation networks in single crystallites are presented. First, the explicit expression for the area swept by a FR source pre-, at- and post-yield is derived. Secondly, the geometries of the slip systems in FCC and BCC single crystallites are incorporated. Making use of well known methods from linear elastic theory, we visualize the apparent elastic constants.

It is shown that the previously predicted isotropic tangent modulus by Van Liempt and Sietsma [8] only yields accurate results for highly compressible material. For a finite Poisson's ratio, previous analysis was prone to over- and/or underestimate the total dislocation density and effective segment length. Varying the dislocation density across slip systems to describe a (non)uniform dislocation distribution, we observe:

- The pre-yield mechanical response for a given dislocation network in a linear elastic isotropic material is anisotropic. The anisotropic symmetry and the magnitude of anisotropy depend on the dislocation distribution, density and character;
- The initial moduli depend on the ratio between edge and screw dislocations for a finite Poisson's ratio. They decrease with increasing edge dislocation density and Poisson's ratio. For incompressible solids with a finite edge dislocation density, the apparent initial Young's modulus vanishes;
- The yield strength of single crystals depends on the initial lengths of edge or screw dislocation segments. The anelastic dislocation strain increases with (edge) dislocation density. Hence the total principal strain at yield cannot be predicted by the linear elastic stiffness alone.

In this work, the fundamental understanding on the effects of dislocation network geometry on the pre- and at-yield constitutive behaviour is expanded. The obtained knowledge will aid in the future design of forming methods [12] and micro-mechanical systems [13]. The main contribution is incorporating dislocation densities with varying character in predicting the pre-yield mechanical behaviour of materials with a generic Poisson's ratio. Dislocation character has major effects on both the apparent elastic constants and yield points. This suggests that reassessment of studies on aforementioned topics is appropriate. Current limitations on *e.g.* the distribution of dislocation links lengths, (far-field) elastic interaction and equivalent isotropic elasticity, are readily lifted by the Dislocation Dynamic Method [63]. Present model though is of engineering interest in higher scale computational methods under static loading conditions. The model's ulterior application is to experimentally obtain information on the geometry of an *a priori* unknown dislocation network. We find that near-incompressible materials and aluminum are promising candidates for future experimental research.

Declaration of Competing Interest

The authors declare that they have no known competing financial interests or personal relationships that could have appeared to influence the work reported in this paper.

Acknowlgedgments

This research was carried out under project number T17019n in the framework of the Research Program of the Materials innovation institute (M2i) (www.m2i.nl) supported by the Dutch government.

Appendix A. Frank-Read source

A1. Equilibrium shapes

The loci of the pinning points are given by

$$\left\{\frac{x_\alpha(\phi_\alpha)}{L}, \frac{y_\alpha(\phi_\alpha)}{L}\right\} \equiv \left\{-\frac{\cos(\phi_\mathrm{i})}{2}, \frac{\sin(\phi_\mathrm{i})}{2}\right\}, \tag{A.1a}$$

and

$$\left\{\frac{x_\beta(\phi_\beta)}{L}, \frac{y_\beta(\phi_\beta)}{L}\right\} \equiv \left\{\frac{\cos(\phi_\mathrm{i})}{2}, -\frac{\sin(\phi_\mathrm{i})}{2}\right\}. \tag{A.1b}$$

Hence the scaled integration constants are

$$\frac{C_1}{L} = -\frac{\tau_\mathrm{c}}{8\tau'_{xz}}\left(4\sin(\phi_\alpha) + \nu\sin(\phi_\alpha) + \nu\sin(3\phi_\alpha)\right) - \frac{\cos(\phi_\mathrm{i})}{2}, \tag{A.2a}$$

and

$$\frac{C_2}{L} = -\frac{\tau_\mathrm{c}}{8\tau'_{xz}}\left(4\cos(\phi_\beta) - 5\nu\cos(\phi_\beta) + \nu\cos(3\phi_\beta)\right) - \frac{\sin(\phi_\mathrm{i})}{2}. \tag{A.2b}$$

Combining Eqs. (A.1) and (A.2), we give the coordinates along the dislocation loop as

$$\frac{x(\phi)}{L} \equiv \frac{\tau_\mathrm{c}}{8\tau'_{xz}}\left((4\sin(\phi) + \nu\sin(\phi) + \nu\sin(3\phi)) - \left(4\sin(\phi_\alpha) + \nu\sin(\phi_\alpha) + \nu\sin(3\phi_\alpha)\right)\right) - \frac{\cos(\phi_\mathrm{i})}{2}; \tag{A.3a}$$

$$\frac{y(\phi)}{L} \equiv \frac{\tau_\mathrm{c}}{8\tau'_{xz}}\left((4\cos(\phi) - 5\nu\cos(\phi) + \nu\cos(3\phi)) - \left(4\cos(\phi_\beta) - 5\nu\cos(\phi_\beta) + \nu\cos(3\phi_\beta)\right)\right) - \frac{\sin(\phi_\mathrm{i})}{2}. \tag{A.3b}$$

Using Eqs. (A.6) and (A.9), we obtain the normalised equilibrium shape of the initial RHS dislocation segment as

$$\frac{x(\phi)}{L} = \frac{4\sin(\phi) + \nu\sin(\phi) + \nu\sin(3\phi)}{2\left(4\sin(\Delta\phi_\mathrm{s}) + \nu\sin(\Delta\phi_\mathrm{s}) + \nu\sin(3\Delta\phi_\mathrm{s})\right)}; \tag{A.4a}$$

$$\frac{y(\phi)}{L} = \frac{4\cos(\phi) - 5\nu\cos(\phi) + \nu\cos(3\phi) - \left(4\cos(\Delta\phi_\mathrm{s}) - 5\nu\cos(\Delta\phi_\mathrm{s}) + \nu\cos(3\Delta\phi_\mathrm{s})\right)}{2\left(4\sin(\Delta\phi_\mathrm{s}) + \nu\sin(\Delta\phi_\mathrm{s}) + \nu\sin(3\Delta\phi_\mathrm{s})\right)}, \tag{A.4b}$$

and the normalised equilibrium of the initial positive edge dislocation segment as

$$\frac{x(\phi)}{L} = \frac{4\sin(\phi) + \nu\sin(\phi) + \nu\sin(3\phi) - \left(4\cos(\Delta\phi_\mathrm{e}) + \nu\cos(\Delta\phi_\mathrm{e}) - \nu\cos(3\Delta\phi_\mathrm{e})\right)}{2\left(4\sin(\Delta\phi_\mathrm{e}) - 5\nu\sin(\Delta\phi_\mathrm{e}) - \nu\sin(3\Delta\phi_\mathrm{e})\right)}; \tag{A.5a}$$

$$\frac{y(\phi)}{L} = \frac{4\cos(\phi) - 5\nu\cos(\phi) + \nu\cos(3\phi)}{2\left(4\sin(\Delta\phi_\mathrm{e}) - 5\nu\sin(\Delta\phi_\mathrm{e}) - \nu\sin(3\Delta\phi_\mathrm{e})\right)}. \tag{A.5b}$$

A2. Pure character angles

For initial pure screw character segments, Eq. (6) is rewritten as

$$\frac{\tau'_{xz}}{\tau_c} = \sin\left(\Delta\phi_s\right) + \nu\sin\left(\Delta\phi_s\right) - \nu\sin^3\left(\Delta\phi_s\right). \tag{A.6}$$

We are interested in the difference angle $\Delta\phi_{\bullet}$ as an explicit function of the shear stress τ_{xz}, for which we substitute $s \equiv \sin\left(\Delta\phi_{\bullet}\right)$. Rearranging Eq. (A.6), we find a convenient form to determine the three roots s_g, with subscript $g = 0, 1$ and 2, being

$$0 = s_g^3 - \left(1 + \frac{1}{\nu}\right)s_g + \frac{1}{\nu}\frac{\tau'_{xz}}{\tau_c}. \tag{A.7}$$

The three real-valued roots of a cubic equation [64]

$$0 = r^3 + pr + q, \tag{A.8a}$$

are

$$r_g \equiv 2\sqrt{-\frac{p}{3}}\cos\left(\frac{1}{3}\cos^{-1}\left(\frac{3q}{2p}\sqrt{-\frac{3}{p}}\right) - \frac{2\pi g}{3}\right), \quad \text{when} \quad p < 0. \tag{A.8b}$$

Substituting Eq. (A.7) in Eq. (A.8) and noting $\sin\left(\Delta\phi_s\right) \in [-1, 1]$, we find $g = 1$ and the explicit equation of the difference angle for the stable equilibrium shape $\Delta\phi_s$.

For initial pure edge character segments, Eq. (11) is rewritten as

$$\frac{\tau_{xz}}{\tau_c} = \frac{1}{4(1-\nu)}\left(4\sin\left(\Delta\phi_e\right) - 5\nu\sin\left(\Delta\phi_e\right) - \nu\sin\left(3\Delta\phi_e\right)\right), \tag{A.9a}$$

and

$$\frac{\tau_{xz}}{\tau_c} = \frac{\sin\left(\Delta\phi_e\right)}{1-\nu} - \frac{2\nu\sin\left(\Delta\phi_e\right)}{1-\nu} + \frac{\nu\sin^3\left(\Delta\phi_e\right)}{1-\nu}. \tag{A.9b}$$

Rearranging Eq. (A.9b), we find a convenient form to determine the three roots s_g of the cubic equation:

$$0 = s_g^3 + \left(\frac{1}{\nu} - 2\right)s_g + \frac{(\nu-1)}{\nu}\frac{\tau_{xz}}{\tau_c}, \tag{A.10}$$

which is of the same form as Eq. (A.8a), but with $p \geq 0$, since $\nu \leq 1/2$. The single real-valued and two complex-valued roots of the cubic equation (A.8a) [64] for $p > 0$ are

$$r_g = 2\sqrt{\frac{p}{3}}\sinh\left(\frac{1}{3}\sinh^{-1}\left(-\frac{3q}{2p}\sqrt{\frac{3}{p}}\right) + \frac{2i\pi g}{3}\right), \tag{A.11}$$

where i is the imaginary unit. Substituting Eq. (A.10) in (A.8a) and (A.11), and noting $\sin\left(\Delta\phi_e\right) \in [-1, 1]$, we use $g = 0$ and find the explicit equation of the difference angle for the stable equilibrium shape $\Delta\phi_e$.

A3. Swept areas

Considering a FR source with generic initial dislocation character ϕ_i, we substitute Eq. (A.2) in Eq. (4) and, noting

$$\begin{aligned}
&\frac{1}{L^2}\left(x(\phi)\frac{\partial y(\phi)}{\partial\phi} - y(\phi)\frac{\partial x(\phi)}{\partial\phi}\right) = \frac{2-\nu+3\nu\cos(2\phi)}{32}\left(\frac{\tau_c}{\tau'_{xz}}\right)^2\\
&\left(\cos(\phi)\left(2\nu\cos(\phi) + (4-5\nu)\cos\left(\phi_\beta\right) + \nu\cos\left(3\phi_\beta\right) + 4\frac{\tau'_{xz}}{\tau_c}\sin\left(\phi_i\right)\right)\right.\\
&\left.+\sin(\phi)\left(-2\nu\sin\left(\phi+(\nu+4)\sin\left(\phi_\alpha\right)+\nu\sin\left(3\phi_\alpha\right)+4\frac{\tau'_{xz}}{\tau_c}\cos\left(\phi_i\right)\right)\right)+2\nu-4\right),
\end{aligned} \tag{A.12}$$

obtain the normalised area swept out as

$$\begin{aligned}
\frac{S(\phi_\alpha,\phi_\beta)}{L^2} = \frac{1}{256}\left(\frac{\tau_c}{\tau'_{xz}}\right)^2 &(16(2(\phi_\beta-\phi_\alpha)+4\sin(\phi_\alpha)\cos(\phi_\beta)\\
&-\sin(2\phi_\alpha)-\sin(2\phi_\beta))-8\nu(\sin(4\phi_\alpha)+\sin(4\phi_\beta)\\
&+4(\phi_\beta-\phi_\alpha-\sin(2\phi_\beta)+2\sin(\phi_\alpha)\cos(\phi_\beta))\\
&-2(\sin(\phi_\alpha)\cos(3\phi_\beta)+\sin(3\phi_\alpha)\cos(\phi_\beta)))\\
&+8\frac{\tau'_{xz}}{\tau_c}(4\cos(\phi_\beta+\phi_i)-2\nu\cos(\phi_\beta+\phi_i)-2(2-\nu)\cos(\phi_\alpha+\phi_i)\\
&+3\nu(\cos(\phi_i-\phi_\alpha)-\cos(\phi_i-\phi_\beta))+\nu(\cos(3\phi_\beta+\phi_i)\\
&-\cos(3\phi_\alpha+\phi_i)))+\nu^2(4(\phi_\alpha-\phi_\beta)+3\sin(2\phi_\beta)+19\sin(2\phi_\alpha)\\
&+\sin(4\phi_\beta)+7\sin(4\phi_\alpha)-\sin(6\phi_\alpha)-\sin(6\phi_\beta)+4(\sin(\phi_\alpha)\cos(3\phi_\beta)\\
&+\sin(3\phi_\alpha)\cos(3\phi_\beta))-20(\sin(\phi_\alpha)\cos(\phi_\beta)+\sin(3\phi_\alpha)\cos(\phi_\beta))).
\end{aligned} \tag{A.13}$$

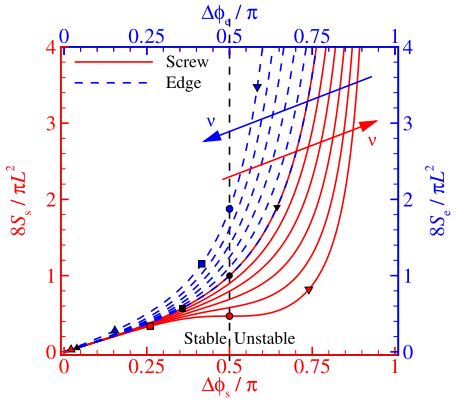

Fig. A.13. The normalised swept-out areas $8S_S/\pi L^2$ and $8S_e/\pi L^2$ as a function of the normalised difference angles $\Delta\phi_s/\pi$ and $\Delta\phi_e/\pi$ for Poisson's ratios $\nu = 0,\ 1/10,\ 1/5,\ 3/10,\ 2/5$ and $1/2$. The coloured arrows indicate an increase in Poisson's ratio ν across equivalently coloured lines.

Hereby, the normalised area swept by the RHS screw FR source is

$$\begin{aligned}
\frac{S_s\left(\Delta\phi_s\right)}{L^2} = &\frac{1}{32\left(2+\nu+\nu\cos\left(2\Delta\phi_s\right)\right)^2\sin^2\left(\Delta\phi_s\right)}((32-32\nu-4\nu^2)\Delta\phi_s\\
&-(16-32\nu-3\nu^2)\sin(2\Delta\phi_s)-(8\nu-\nu^2)\sin(4\Delta\phi_s)\\
&-\nu^2\sin(6\Delta\phi_s)),
\end{aligned} \tag{A.14}$$

and for the positive edge FR source

$$\begin{aligned}
\frac{S_e\left(\Delta\phi_e\right)}{L^2} = &\frac{1}{32\left(\nu\cos\left(3\nu+2\Delta\phi_e\right)-2\right)^2\sin^2\left(\Delta\phi_e\right)}\left(\left(32-32\nu-4\nu^2\right)\Delta\phi_e\right.\\
&-(16-19\nu^2)\sin(2\Delta\phi_e)+(8\nu-7\nu^2)\sin(4\Delta\phi_e)\\
&\left.-\nu^2\sin(6\Delta\phi_e)\right).
\end{aligned} \tag{A.15}$$

Equations (A.14) and (A.15) are equivalent to the swept areas Cash and Cai [14] obtained apart from different definitions of difference angle. The area swept $S(\Delta\phi)$ is given in Fig. A.13. For the ease of comparison with Figs. 3a and 3b, the swept areas, which correspond to line stresses $\tau_{xz}/\tau_c = \tau'_{xz}/\tau_c = 1/10,\ 9/10$ and 1 are indicated with (coloured) triangle, square, circle and gradient symbols as well in Fig. A.13.

Appendix B. Taylor factor

Using the principle of virtual work, we require that the rate of external anelastic work is equivalent to the rate of internal anelastic work across k slip systems, i.e.

$$\boldsymbol{\sigma} : \frac{\partial\epsilon^{an}}{\partial t} \equiv \sum_k \left|\tau_{xz}\frac{\partial\gamma^{an}_{xz}}{\partial t}\right|, \tag{B.1}$$

where τ_{xz} and γ^{an}_{xz} are the shear stress and anelastic shear strain, respectively, and their magnitudes may vary between slip systems. It is convenient to express the rate of external anelastic work in terms of the principal deformation rates by

$$\frac{\partial W^{an}}{\partial t} = \left|\frac{\partial\epsilon^{an}_1}{\partial t}\left(\sigma_1 + \lambda\sigma_2 + (1-\lambda)\sigma_3\right)\right|, \tag{B.2a}$$

with contraction ratio $\lambda \equiv \partial\epsilon_2^{an}/\partial\epsilon_1^{an}$ and conservation of volume during dislocation glide, i.e.

$$\frac{\partial\epsilon_2^{an}}{\partial t} + \frac{\partial\epsilon_2^{an}}{\partial t} + \frac{\partial\epsilon_2^{an}}{\partial t} \equiv 0, \tag{B.2b}$$

where $|\frac{\partial\epsilon_1^{an}}{\partial t}| \geq |\frac{\partial\epsilon_2^{an}}{\partial t}| \geq |\frac{\partial\epsilon_3^{an}}{\partial t}|$ are the absolute principal strain rates. In a virtual tensile test, there is a single principal stress component and we rewrite Eq. (B.1) as a function of the normal stress

$$\sigma\frac{\partial\epsilon^{an}}{\partial t} = \sum_k \left|\tau_{xz}\frac{\partial\gamma_{xz}^{an}}{\partial t}\right|. \tag{B.3a}$$

Following Van Liempt and Sietsma [8] and using the Taylor factor M, we relate the normal stress to the resolved shear stress τ in each grain by

$$M \equiv \frac{\sigma}{\tau} = \sum_k \frac{\partial\gamma_{xz}^{an}}{\partial\epsilon^{an}}. \tag{B.3b}$$

Furthermore, we assume: (1) each grain is subjected to a normal stress parallel to the tensile axis [45]; (2) all orientations are equally likely [45]; (3) the resolved shear stress τ is the same in each grain [8]; and (4), each grain extends by the same amount along the tensile axis [44]. Integrating the right-hand side of Eq. (B.3b) with the boundary condition $\gamma_{xz}^{an}(0) \equiv 0$ for no applied principal strain, we obtain

$$\tau = \frac{\sigma}{M}, \qquad \text{and} \qquad \epsilon^{an} = \frac{1}{M}\sum_k \gamma_{xz}^{an}. \tag{B.4}$$

Supplementary material

Supplementary material associated with this article can be found, in the online version, at doi:10.1016/j.mtla.2021.101178.

References

[1] U. Kocks, H. Mecking, Physics and phenomenology of strain hardening: the fcc case, Prog Mater Sci 48 (3) (2003) 171–273.
[2] Y. Bergström, W. Roberts, The application of a dislocation model to dynamical strain ageing in α-iron containing interstitial atoms, Acta Metall. 19 (8) (1971) 815–823.
[3] P. van Liempt, Yield and flow stress of steel in the austenitic state, Delft University of Technology, 2016 Ph.D. thesis.
[4] F. Roters, D. Raabe, G. Gottstein, Work hardening in heterogeneous alloys-a microstructural approach based on three internal state variables, Acta Mater 48 (17) (2000) 4181–4189.
[5] G. Prasad, M. Goerdeler, G. Gottstein, Work hardening model based on multiple dislocation densities, Materials Science and Engineering: A 400 (2005) 231–233.
[6] J. Koehler, G. DeWit, Influence of elastic anisotropy on the dislocation contribution to the elastic constants, Physical Review 116 (5) (1959) 1121.
[7] B.K. Agrawal, G. Verma, Dislocation contribution to the elastic constants of body–centered cubic crystals, Physical Review 127 (2) (1962) 501.
[8] P. van Liempt, J. Sietsma, A physically based yield criterion I. determination of the yield stress based on analysis of pre-yield dislocation behaviour, Materials Science and Engineering: A 662 (2016) 80–87.
[9] Z. Arechabaleta, P. van Liempt, J. Sietsma, Quantification of dislocation structures from anelastic deformation behaviour, Acta Mater 115 (2016) 314–323.
[10] Z. Arechabaleta, P. van Liempt, J. Sietsma, Unravelling dislocation networks in metals, Materials Science and Engineering: A 710 (2018) 329–333.
[11] J.D. Eshelby, Dislocations as a cause of mechanical damping in metals, Proceedings of the Royal Society of London. Series A. Mathematical and Physical Sciences 197 (1050) (1949) 396–416.
[12] A. Torkabadi, E. Perdahcıoğlu, V. Meinders, A. van den Boogaard, On the nonlinear anelastic behavior of AHSS, Int J Solids Struct 151 (2018) 2–8.
[13] S. Shao, M.M. Khonsari, J. Wang, N. Shamsaei, N. Li, Frequency dependent deformation reversibility during cyclic loading, Materials Research Letters 6 (7) (2018) 390–397.
[14] W. Cash, W. Cai, Dislocation contribution to acoustic nonlinearity: the effect of orientation-dependent line energy, J Appl Phys 109 (1) (2011) 014915.
[15] R.B. Sills, N. Bertin, A. Aghaei, W. Cai, Dislocation networks and the microstructural origin of strain hardening, Phys. Rev. Lett. 121 (8) (2018) 085501.
[16] R. Gasca-Neri, W. Nix, A model for the mobile dislocation density, Acta Metall. 22 (3) (1974) 257–264.
[17] A. Orlová, Two concepts of mobile dislocation density in creep at high temperatures, Materials Science and Engineering: A 151 (2) (1992) 153–160.
[18] G. Pharr, W. Nix, Application of the methods of dislocation dynamics to describe plastic flow in both bcc and fcc metals, Acta Metall. 27 (3) (1979) 433–444.
[19] D. Kuhlmann-Wilsdorf, LEDS: properties and effects of low energy dislocation structures, Materials Science and Engineering 86 (1987) 53–66.
[20] G.I. Taylor, The mechanism of plastic deformation of crystals. Part I.theoretical, Proc. R. Soc. Lond. A 145 (855) (1934) 362–387.
[21] G. Saada, On hardening due to the recombination of dislocations, Acta Metall 8 (1960) 841–847.
[22] A.H. Cottrell, B. Bilby, Dislocation theory of yielding and strain ageing of iron, Proc. Phys. Soc. London, Sect. A 62 (1) (1949) 49.
[23] F. Frank, W. Read Jr, Multiplication processes for slow moving dislocations, Physical Review 79 (4) (1950) 722.
[24] D. Li, R.H. Wagoner, The nature of yielding and anelasticity in metals, Acta Mater 206 (2021) 116625.
[25] G. Schoeck, Dislocation theory of plasticity of metals, in: Advances in applied mechanics, 4, Elsevier, 1956, pp. 229–279.
[26] G. DeWit, J.S. Koehler, Interaction of dislocations with an applied stress in anisotropic crystals, Physical Review 116 (5) (1959) 1113.
[27] I. Kovacs, The critical shear stress needed for the operation of a dislocation segment as a frank-read source in anisotropic crystals, physica status solidi (b) 3 (1) (1963) 140–144.
[28] W. Cai, W.D. Nix, Imperfections in Crystalline Solids, Cambridge University Press, 2016.
[29] F. Yoshida, T. Uemori, K. Fujiwara, Elastic–plastic behavior of steel sheets under in-plane cyclic tension–compression at large strain, Int. J. Plast. 18 (5–6) (2002) 633–659.
[30] L. Sun, R. Wagoner, Complex unloading behavior: nature of the deformation and its consistent constitutive representation, Int. J. Plast. 27 (7) (2011) 1126–1144.
[31] A. Torkabadi, Towards an Accurate Springback Prediction, University of Twente, 2018.
[32] R. Scattergood, D. Bacon, The Orowan mechanism in anisotropic crystals, Philos. Mag. 31 (1) (1975) 179–198.
[33] S.P. Fitzgerald, Frank–read sources and the yield of anisotropic cubic crystals, Philos Mag Lett 90 (3) (2010) 209–218.
[34] S. Fitzgerald, S. Aubry, Self-force on dislocation segments in anisotropic crystals, J. Phys.: Condens. Matter 22 (29) (2010) 295403.
[35] S. Aubry, S. Fitzgerald, S. Dudarev, W. Cai, Equilibrium shape of dislocation shear loops in anisotropic α-Fe, Modell. Simul. Mater. Sci. Eng. 19 (6) (2011) 065006.
[36] S. Fitzgerald, S. Aubry, S. Dudarev, W. Cai, Dislocation dynamics simulation of frank-read sources in anisotropic α-Fe, Modell. Simul. Mater. Sci. Eng. 20 (4) (2012) 045022.
[37] J. Nordmann, M. Aßmus, H. Altenbach, Visualising elastic anisotropy: theoretical background and computational implementation, Continuum Mech. Thermodyn. 30 (4) (2018) 689–708.
[38] P.M. Anderson, J.P. Hirth, J. Lothe, Theory of dislocations, Cambridge University Press, 2017.
[39] W. Cai, A. Arsenlis, C.R. Weinberger, V.V. Bulatov, A non-singular continuum theory of dislocations, J Mech Phys Solids 54 (3) (2006) 561–587.
[40] See Supplementary Material for Analysis and Additional Results.
[41] Q.-C. He, A. Curnier, A more fundamental approach to damaged elastic stress-strain relations, Int J Solids Struct 32 (10) (1995) 1433–1457.
[42] T. Böhlke, C. Brüggemann, Graphical representation of the generalized hookes law, Technische Mechanik 21 (2) (2001) 145–158.
[43] E. Orowan, Problems of plastic gliding, Proceedings of the Physical Society 52 (1) (1940) 8.
[44] A. Kochendorfer, Reine und angewandte metallkunde, Springer Berlin, 1941.
[45] J. Bishop, R. Hill, XLVI. A theory of the plastic distortion of a polycrystalline aggregate under combined stresses, The London, Edinburgh, and Dublin Philosophical Magazine and Journal of Science 42 (327) (1951) 414–427.
[46] H. Frost, M. Ashby, Deformation-mechanism Maps for Pure Iron, Two Austenitic Stainless Steels, and a Low-alloy Ferritic Steel, in: Fundamental aspects of structural alloy design, Springer, 1977, pp. 27–65.
[47] H. Zurob, C. Hutchinson, Y. Brechet, G. Purdy, Modeling recrystallization of microalloyed austenite: effect of coupling recovery, precipitation and recrystallization, Acta Mater 50 (12) (2002) 3077–3094.
[48] N. Xiao, M. Tong, Y. Lan, D. Li, Y. Li, Coupled simulation of the influence of austenite deformation on the subsequent isothermal austenite–ferrite transformation, Acta Mater 54 (5) (2006) 1265–1278.
[49] K. Levenberg, A method for the solution of certain non-linear problems in least squares, Q top Q. Appl. Math. 2 (2) (1944) 164–168.
[50] D.W. Marquardt, An algorithm for least-squares estimation of nonlinear parameters, Journal of the society for Industrial and Applied Mathematics 11 (2) (1963) 431–441.
[51] D. Kuhlmann-Wilsdorf, Unified theory of stages II and III of workhardening in pure FCC metal crystals, Technical Report, Virginia Univ., Charlottesville. School of Engineering and Applied Science, 1966.
[52] Z.A. Lethbridge, R.I. Walton, A.S. Marmier, C.W. Smith, K.E. Evans, Elastic anisotropy and extreme Poissons ratios in single crystals, Acta Mater 58 (19) (2010) 6444–6451.
[53] C.M. Kube, Elastic anisotropy of crystals, AIP Adv 6 (9) (2016) 095209.
[54] E. Schmid, W. Boas, Kristallplastizität mit besonderer Berücksichtigung der Metalle, 17, Springer-Verlag, 2013.
[55] N. Brown, R. Ekvall, Temperature dependence of the yield points in iron, Acta Metall. 10 (11) (1962) 1101–1107.
[56] A. De Vaucorbeil, W. Poole, C. Sinclair, The superposition of strengthening contributions in engineering alloys, Materials Science and Engineering: A 582 (2013) 147–154.

[57] L.P. Kubin, R. Madec, B. Devincre, Dislocation intersections and reactions in FCCand BCC crystals, MRS Online Proceedings Library Archive 779 (2003).
[58] G. Po, Y. Cui, D. Rivera, D. Cereceda, T.D. Swinburne, J. Marian, N. Ghoniem, A phenomenological dislocation mobility law for bcc metals, Acta Mater 119 (2016) 123–135.
[59] C. Zener, Contributions to the theory of beta-phase alloys, Physical Review 71 (12) (1947) 846.
[60] W. Voigt, et al., Lehrbuch der kristallphysik, 962, Teubner Leipzig, 1928.
[61] A. Reuß, Berechnung der fließgrenze von mischkristallen auf grund der plastizitätsbedingung für einkristalle, ZAMM-Journal of Applied Mathematics and Mechanics/Zeitschrift für Angewandte Mathematik und Mechanik 9 (1) (1929) 49–58.
[62] D. Dever, Temperature dependence of the elastic constants in α-iron single crystals: relationship to spin order and diffusion anomalies, J Appl Phys 43 (8) (1972) 3293–3301.
[63] N. Bertin, R.B. Sills, W. Cai, Frontiers in the simulation of dislocations, Annu Rev Mater Res 50 (2020) 437–464.
[64] G. Birkhoff, S. Mac Lane, A Survey of Modern Algebra, Universities Press, 1998.